Freeze-thaw effects on the performance of TRM-strengthened masonry

Dalalbashi, Ali; Ghiassi, Bahman; Oliveira, Daniel V.

DOI:
10.1016/j.jobe.2022.105077

Freeze-thaw effects on the performance of TRM-strengthened masonry

Ali Dalalbashi[1], Bahman Ghiassi[2], Daniel V. Oliveira[3]

ABSTRACT

In recent years, textile-reinforced mortars (TRMs) have been introduced as a sustainable and effective mean of strengthening masonry and concrete structures. Although many recent studies have focused on understanding the mechanical performance of TRM composites and TRM-strengthened masonry panels, their long-term durability has remained unexplored. This article presents a multi-level experimental and analytical investigation on the effect of freeze-thaw conditions on the behavior of masonry components strengthened with TRMs. The adopted TRM strengthening system is composed of an AR-glass fabric reinforced embedded in a hydraulic lime-based mortar. The tests include characterization of the changes in material properties, TRM tensile behavior, the fabric-to-mortar and the TRM-to-substrate bond behavior, and finally, the in-plane and the out-of-plane response of TRM-strengthened masonry panels after exposure to freeze-thaw cycles. The results reveal that although deterioration of properties at the composite level is observed, the considered freeze-thaw cycles did not affect the in-plane and out-of-plane performance of the strengthened panels.

Keywords: Durability; Freeze-Thaw; Masonry; Multi-level testing; TRM.

[1] PhD student, ISISE, Department of Civil Engineering, University of Minho, Guimarães, Portugal. E-mail: alidalalbashi@gmail.com. https://orcid.org/0000-0003-0486-1433

[2] Associate Professor, School of Engineering, University of Birmingham, Birmingham, United Kingdom. E-mail: b.ghiassi@bham.ac.uk. http://orcid.org/0000-0003-4212-8961

[3] Associate Professor, ISISE, Department of Civil Engineering, University of Minho, Guimarães, Portugal. E-mail: danvco@civil.uminho.pt. http://orcid.org/0000-0002-8547-3805

1 Introduction

The catastrophic failure or collapse of unreinforced masonry (URM) structures after earthquakes and the responsible mechanisms for that have been extensively reported in previous literature [1,2]. To protect these structures against this key natural hazard, many previous studies have focused on the development of strengthening strategies to improve the seismic behavior and safety of masonry structures. One of the most common strengthening methods is externally bonded reinforcement, in which the repair material (usually a composite) is attached to the external surface of structural elements [3,4]. For many years, fiber-reinforced polymers (FRPs) were the primary strengthening material of this strengthening method [5–7]. Although the application of FRPs on external surfaces of walls improves the seismic performance of masonry structures, issues related to sustainability, durability, and compatibility highlighted the need to develop novel repair materials for this purpose.

Textile-reinforced mortar (TRM) composites have recently received extensive attention as a suitable alternative to FRP composites due to their fire resistance, sustainability, and better mechanical and hygral compatibility with masonry substrates [8–11]. TRM composites, also referred to as FRCM, are continuous textile meshes or grids (made of carbon, basalt, steel, glass, or natural fibers) embedded in an inorganic matrix (e.g., cement or lime-based mortars) [1,12]. The performance of TRMs as a repair material is highly dependent on the bond behavior at the textile-to-mortar (usually assessed through pull-out tests [13–15]) and TRM-to-substrate interface (usually assessed through shear debonding tests [16–18]), as well as the mechanical properties of its constituents [19,20]. TRM composites can be developed with a wide range of mechanical properties due to the variety of fabrics and mortars available. A properly designed TRM shows a pseudo-ductile response (in tensile and/or flexural tests [21–23]) with distributed cracking, which is helpful in seismic strengthening applications [24,25]. Recent but still limited experimental and computational studies have shown promising results on the effectiveness of TRMs in improving the in-plane [26–30] and out-of-plane [29,31,32] performance of masonry components. While further studies are still needed to better understand the governing mechanisms of these composites under complex loading conditions, there is also a lack of knowledge on the durability and long-term performance of TRMs and TRM-strengthened masonry components [33,34]. Durability studies are still scarce and limited to few studies investigating the role of saline, alkaline, or natural aging on the mechanical properties of TRMs, textile-to-mortar interface, or TRM-strengthened masonry interface [35–38]. Also, a few studies are available in which the bond behavior [39,40] and mechanical properties (tensile and flexural strength) [41–45] of TRM composites under freeze-thaw (FT) conditions were investigated. TRM composites showed either improvement [44,45] or decline [39–43] in bond and mechanical behavior, regardless of the number of FT cycles applied to the specimens. Furthermore, FT conditions resulted in a slight decrease in the out-of-plane behavior of TRM-strengthened masonry panels [46]. However, comprehensive studies from materials to masonry panel scale that allow a full understanding of how these repair systems perform under different environmental conditions are still missing.

This paper presents an experimental study on the changes in the mechanical performance of TRM-strengthened masonry after exposure to FT conditions. The tests are performed at different levels, from material to composite and masonry panel level, aiming at providing a better understanding of the role of different parameters on the durability of these systems. A commercial glass-based TRM composite (made of a bidirectional AR-glass and hydraulic lime-based mortar) commonly used to strengthen existing and traditional masonry structures is used for this purpose. The obtained results presented and discussed in this paper contribute to a better understanding of the long-term performance of these systems and the structures reinforced with them.

2 Experimental program

A series of TRM composite specimens were prepared (details can be found in sections 2.1 to 2.8). After 90 days of curing at laboratory conditions, the specimens were subjected to zero (as reference), 60, 120, 180, 240, 300, and 360 FT cycles. A series of mechanical/physical characterization tests were performed at the material level (i.e., compressive, flexural, and tensile tests on bricks, mortar, and fabrics), at the materials interfaces (fiber-to-mortar and TRM-to-substrate bond test), at the composite level (TRM tensile test), and at the masonry panel level (diagonal compression and out-of-plane bending tests on TRM-strengthened masonry) to investigate the FT induced deterioration mechanisms across scales. This section presents a detailed description of materials, preparation of specimens, and the test methods, see also Table 1. Fig. 1 shows the timeline used to prepare and test the samples to understand the framework's sequences and logic.

The specimens at the composite and masonry panel levels are labeled as XYZ and VVYZ, respectively. X is related to the type of micro- and meso-level tests (T: Tensile test of TRM, P:

Pull-out, S: Single-lap shear). VV is linked to the kind of panel (UD and SD: Unreinforced and Strengthened Diagonal compression, UP and SP: Unreinforced and Strengthened out-of-plane failure parallel to bed joint, UN and SN: Unreinforced and Strengthened out-of-plane failure normal to bed joint, respectively). Y is related to the control (C) or exposed (E) specimens, and Z is connected to the number of FT cycles. For example, PE360 is a pull-out specimen exposed to 360 FT cycles.

2.1 Materials

The TRM composite was produced from a commercial hydraulic mortar (named mortar M1) as the matrix and a glass fabric as the reinforcement. The commercial fabric was a woven biaxial fabric mesh of alkali-resistance (AR) glass. Its mesh size and area per unit length were 25×25 mm^2 and 35.27 mm^2/ m, respectively (see Fig. 2a). A commercial lime and ecopozzolan mortar, referred to as mortar M2, was used for the masonry joints and solid clay bricks (200×100×50 mm) were used as units.

2.2 Specimens preparation and curing procedures

The masonry panels were prepared and cured in the lab conditions (18°C, 75% RH) for thirty days. Then, half of them were strengthened with the TRM strengthening system and covered with wet clothes and plastic for seven days. Material and bond characterization specimens were also prepared and cured following the same procedure (covering with wet clothes and plastic for seven days). All the molded samples were demolded after three days. The specimens were then kept in the lab environment until the test date or exposure to FT cycles. The samples constructed with mortar M1 were stored in the lab for 90 days. Since the panels were strengthened after 30 days of construction, the specimens made with mortar M2 were stored in the lab for 120 days (30 +90 days), as shown in Fig. 1. Afterwards, the specimens were divided into two groups. A part of the specimens was stored in the climatic chamber room to expose them to FT cycles, while the others were stored in the lab environment (control specimens) and tested parallel to the exposed samples, as reported in Table 1.

2.3 Materials characterization tests

The coefficient of thermal expansion (CTE) of the mortar M1 (matrix of the TRM composite) and the brick was calculated according to the method presented in [47]. Since mortar M2 was recommended by the factory for masonry brick work, CET was expected to be in the same range as brick CTE and was not measured. CTE was measured by exposing the specimens to a temperature variation (ΔT= +30 to -10°C) and measuring the length change using a strain gauge. Mortar specimens were prismatic, 150×70×10 mm, and tested after 90 days of curing. Strain gauges were installed on the flatwise surface of the samples. The CTE was computed as $\Delta\varepsilon / \Delta T$, where $\Delta\varepsilon$ is the strain variation of the specimen under temperature change.

The compressive, flexural, and splitting tensile strength, as well as elastic modulus of mortars (M1 and M2), were experimentally determined, according to ASTM C109 [48], EN 1015-11 [49], EN 12390-13 [50], and ASTM C496 [51], respectively. The compressive specimens were cubes (50×50×50 mm^3), the flexural specimens had a prismatic shape (40×40×160 mm^3), and the specimens prepared for measurement of the elastic modulus and tensile splitting strength were cylinders with a diameter of 70 mm and a height of 150 mm (see Fig. 2).

The compressive strength of the bricks was characterized according to ASTM C67 [52] and EN 772-1 [53] and perpendicular to the flatwise direction. The flexural strength and elastic modulus (Fig. 2f) of the brick were calculated according to EN 1015-11 [49] and EN 12390-13 [50], respectively, by using prismatic specimens (40×40×160 mm^3). For measuring the flexural strength and the elastic modulus, the load was applied perpendicular to the flatwise and widthwise surface of the brick.

A Lloyd testing machine was used to perform the compressive and flexural tests under force-controlled conditions at a rate of 150 N/s and 10 N/s, respectively. The elastic modulus was characterized by a universal testing machine (load capacity of 100 kN) and LVDTs (3 for cylinder specimens and 4 for prismatic specimens) with a 5 mm range and 1-µm sensitivity. The universal testing machine was also used to measure mortars' tensile splitting strength under displacement-controlled conditions at a rate of 0.12 mm/min.

The compressive strength of masonry prisms was characterized according to ASTM C1314 [54]. The prisms were constructed by three bricks and 20 mm bed joint mortar (M2), as shown in Fig. 2g. These were performed using a universal testing machine (load capacity of 1000 kN) and introducing monotonic displacements at a rate of 0.3 mm/min.

The fabrics' tensile strength, strain, and elastic modulus were measured through direct tensile tests in both warp and weft directions (Fig. 2h). The tests were performed on single yarns with a free length of 300 mm and using a universal testing machine (load capacity of 10 kN, and under displacement-controlled conditions at a rate of 0.3 mm/min). A 100 mm clip gauge was located at the specimen center, and the internal LVDT of the machine measured the yarn deformation during the tests.

2.4 Pull-out test

The pull-out specimens were prepared by embedding single glass yarns (warp direction) in the mortar M1 with a rectangular cross-sectional area (125×16 mm), as shown in (Fig. 3a). The considered embedded length was 50 mm, which was equal to the effective bond length of the samples [13]. Before this, an epoxy resin prism (10×16×200 mm) was used to protect the free end of the yarn, according to [55]. The yarn-to-mortar bond behavior was investigated by performing the single-sided pull-out test developed in [55]. Two U-shape steel supports attached to a rigid frame fixed the pull-out specimen, and a servo-hydraulic system (load capacity of 25 kN) was used to pull the epoxy resin (and the yarn) from the top with a mechanical clamp under displacement-controlled conditions at a rate of 1.0 mm/min, based on [56], (see Fig. 3a). The yarn-to-mortar slip was measured using three LVDTs with a 20 mm range and a 2-μm sensitivity. The average of LVDTs was presented as the slip in the experimental results.

2.5 TRM tensile tests

Direct tensile tests were conducted on prismatic specimens (550×70×10 mm), in which three warp and 13 weft glass yarns were embedded in the mortar M1 (Fig. 3b). Seven days before the tests, the free parts of the yarns were saturated with resin, followed by attaching two steel plates (100×75×10 mm) to prevent rapture of the yarns in the clamping area during the tests [29]. As shown in Fig. 3b, two mechanical clamps gripped the samples (clamping-grip configuration). A servo-hydraulic jack (load capacity of 25 kN) applied the direct tensile load through the clamps under displacement-controlled conditions at a rate of 0.3 mm/min, based on [17]. Also, two LVDTs with a 20 mm range and 2-μm sensitivity recorded the deformation placed at both sides of the specimen.

2.6 Single-lap shear tests

Single-lap shear tests were performed to characterize the TRM-to-substrate bond behavior. The bricks were sandblasted in the flatwise direction to improve the bond at the interface of the TRM composite and brick [29]. Further, the bricks were pre-wetted for one hour before construction to ensure a semi-saturated condition to enhance the TRM-to-substrate bond [29]. These specimens were prepared using the TRM composite on the bricks' flatwise surface. The TRM composite had a 70 mm width, a 10 mm thickness, and a 100 mm length (equal to the embedded length of yarns). The embedded fabric had three warp and weft yarns, as shown in Fig. 3c. Like the TRM tensile specimens, a week before the test dates, the free length of the yarns (315 mm) was saturated with resin, followed by the attachment of aluminum plates (65×65×2 mm) to facilitate gripping and to ensure a uniform load transfer.

The test setup consisted of a rigid supporting frame, two clamps (supported the specimen), a servo-hydraulic system (load capacity of 50 kN), and two LVDTs with a 20 mm range and 2-μm sensitivity (placed at the loaded end to measure the slip during the tests), as shown in Fig. 3c. The tests were performed under displacement-controlled conditions at a rate of 0.3 mm/min [17]. Before starting the tests, a 100 N preload was applied to the specimens to facilitate the LVDTs attachment, as reported in [29].

2.7 Masonry panels

Masonry panels were made with solid clay bricks and mortar M2 (for the joints) for diagonal compression and bending testing. The dimensions of the panels used for diagonal compression tests were 540×540×100 mm (see Fig. 4a), while those used for bending tests were 540×420×100 mm and 520×330×100 mm in the samples loaded to fail parallel to and normal to the bed joints, respectively (Fig. 4b and Fig. 4c). Again, similar to the single-lap shear tests, the bricks were sandblasted (at the lengthwise direction) and pre-wetted for one hour before the construction and application of TRM composites.

The diagonal compression samples were strengthened with TRM on both sides, while the bending panels were reinforced with TRM only on one side of the panels (opposite side of the loading). In all bending panels, the warp yarns were parallel to the longitudinal axis of the specimens. The TRM consisted of 17 and 12 warp yarns in the bending panels with parallel and normal failure to bed joints, respectively, while the weft yarns were 21 in both types of panels.

Diagonal compression tests were performed according to ASTM E519 [57]. The test setup consisted of two rigid steel shoes (115×115×15 mm) placed at the diagonally opposing bottom and top corners of the panels. Four LVDTs with a 20 mm range and 2-μm sensitivity located at both sides of the panels (in 500 mm gauge length) measured the vertical and horizontal deformation of the panels during the tests (Fig. 4 a). A servo-hydraulic system (load capacity of 300 kN) was used to conduct these tests under displacement-controlled conditions and at a rate of 0.3 mm/min, based on [29].

The bending tests were performed according to EN 1052-2 [58]. All the panels were tested vertically and under four-point bending conditions, as shown in Fig. 4b and Fig. 4c. The bending tests consisted of an outer (420 mm) and an inner (170 mm) bearing supports and four LVDTs with a 20 mm range and 2-µm sensitivity to measure the sample deformation at the middle and the location of the inner bearings. A servo-hydraulic system (load capacity of 50 kN) applied the load under displacement-controlled conditions and at a rate of 0.3 mm/min.

2.8 Freeze-thaw (FT) exposure

A Fitoclima 6400 EC25 climate chamber was used for performing the FT tests. The exposure consisted of exposing the samples to 360 cycles consisting of 30°C and 90% relative humidity for two hours, followed by two hours of freezing at -10°C (each cycle lasted 16 hours). This exposure regime was chosen to replicate the conditions considered in [39,59]. As shown in Fig. 5, after every 60 cycles (equal to 40 days) and when the temperature inside the chamber reached 20°C, five samples (from all types except panels, which were only tested after 360 cycles) were taken from the chamber and stored seven days in the lab before conducting the post-exposure tests. In order to avoid any disturbance regarding the transportation of the panels from the climatic chamber to the testing machine, the panels were packed in Styrofoam and plastic and then moved.

3 Results and discussion

3.1 Material characterization results

3.1.1 Coefficient of thermal expansion (CTE)

The CTE of the mortar M1 and the brick were obtained as 20.2×10^{-6}/°C (Coefficient of Variation: CoV= 13%) and 16.5×10^{-6}/°C (CoV= 11%), respectively. This close CTE shows that the two materials are compatible, and the TRM-to-brick interface has a very low probability of cracking due to temperature changes during the FT exposure.

3.1.2 Effect of freeze-thaw (FT) cycles

Table 2 summarizes the variation of material properties under the control and the FT conditions.

Compressive strength. Mortar M1 shows an increment of compressive strength under both control and FT conditions in the first 180 cycles, and then this value drops slightly until the end of the tests (360 cycles). It is interesting to note that the compressive strength of FT exposed M1 specimens at 180 cycles (E180) is similar to those of control samples at the same age (C180, C360, the difference at C360 is about 8% which falls in the range of CoV). Mortar M2, however, shows a reduction of strength under the control conditions and a slight increment of it under the FT conditions. This has led to a 25% higher compressive strength at 360 FT cycles (E360) compared to the control samples at the same age (C360). These observations suggest that higher humidity levels at the exposed environment caused the compressive strength of mortar M1 and M2 to be constant or even slightly higher than the control samples. The compressive strength of the bricks does not show a significant change (4.3% decrease), while the compressive strength of the masonry prism experienced a decrement of around 10% under both the natural and the FT conditions, with the FT exposure having a more deteriorating effect. This result is indeed interesting as both individual mortar and brick samples showed enhancement or no change in the strength after FT exposure conditions. This confirms that the information on the deterioration of individual materials cannot be used to infer the estimation of the deterioration level at the masonry scale.

Flexural strength. The flexural strength of mortar M1 does not change significantly under controlled conditions (it increases 4%), but mortar M2 shows a deterioration of around 20%. Both mortars, however, show a higher flexural strength under FT conditions when compared to control specimens at the same age (M1 shows 6% and 11% higher strength at E360 compared to C360 and C0, respectively). The freeze-thaw conditions were thought to cause microcracks to occur in the flexural specimens and reduce their strength. However, higher humidity in the exposed condition causes the flexural strength of both mortars to increase compared to the control samples. Meanwhile, the bricks' flexural strength is not affected by exposure to FT conditions. These observations are also in line with those made for the compressive strength values mentioned above.

Elastic modulus. The elastic modulus of mortar M1 increased in the first 180 cycles, and then it slightly decreased under the controlled conditions (a total of 20% increase at C360 compared to C0 was observed), but it decreased under the FT conditions until the end of the tests reaching an around 8% smaller value compared to the control samples at the same age. Meanwhile, the elastic modulus of mortar M2 decreased under both control and FT conditions, with the control samples showing a smaller elastic modulus than the FT exposed samples. Microcracks in the exposed specimens may have contributed to the decline of elastic modulus. Yet these microcracks have no bearing on the ultimate compressive and flexural strength of mortars. This should be investigated more in future studies. Again, the bricks' elastic modulus did not change with FT cycles, and those of glass yarns increased.

Tensile splitting strength. The tensile splitting strength of mortar M1 and M2 under controlled conditions was increased 50% and 20%, respectively (C360 compared to C0). Meanwhile, both mortars did not show any change of strength under FT exposure when compared to control samples at the same age (E360 compared to C360). Both mortars' tensile splitting behavior is unaffected by the proposed freeze-thaw conditions, which is consistent with their flexural behavior.

Tensile strength. Finally, the observed changes in the tensile strength of the glass yarns after exposure to FT conditions is negligible (<3%), as expected.

3.2 Yarn-to-mortar bond behavior

Fig. 6a shows the typical pull-out response of all individual specimens at 0 cycles and their experimental averages (of five samples). Moreover, Fig. 6b presents the average load-slip curves of the specimens at 0, 180, and 360 cycles under both control and exposed conditions. In all exposure periods, the load-slip curves show the typical pull-out response. The failure mode for all the specimens was yarn slippage from the mortar, with few exceptions in which the yarn rupture occurs in the post-peak area.

The peak load and debonding energy as the key characteristics of pull-out response are presented in Fig. 6c and d with a linear regression line to demonstrate the general trend of those parameters with age or FT exposure (details given in Table A 1). The debonding energy expresses the energy dissipated during the complete yarn debonding and is defined as the area under the load-slip curve until the peak load [38].

Overall, it can be observed that the peak load of the control samples increases until 180 cycles, and then it decreases significantly until the end of the tests showing a total 40% reduction in PC360 samples compared to PC0. A similar trend is also observed for the debonding energy in the controlled samples. This is however in contrast to the observed changes in the mortar's mechanical properties. All characteristics of the mortar (flexural strength, compressive strength, splitting strength and young modulus) increased until 180 cycles and then rested at that value until 360 cycles. The observed reduction of the peak load in the pull-out tests, therefore, seems not to be explainable by mechanical properties of the mortar obtained from molded large-scale samples (material test samples are at least twice in dimensions compared to pull-out test samples).

The samples exposed to FT conditions, however, do not show any change in the peak load until 180 days of exposure, and then show a drop until the end of the tests reaching the same peak load as controlled specimens at 360 days of exposure. This translates to a 25% reduction of the peak load in PE180 specimens compared to PC180 (noting PE180 is similar to PC0), due to FT exposure. The deterioration induced by FT has diminished after 180 cycles and no significant difference of the peak load is observed in the samples afterwards. This is also interesting as mechanical properties of mortar M1 under FT conditions was generally higher at PE360 compared to PC360 with the exception of the elastic modulus which was 8% smaller. It seems that the combination of strength improvement and elastic modulus reduction has led to achieving a similar peak load in FT exposed samples compared to those of controlled samples at the end of the tests. The debonding energy, however, rests at a lower value compared to controlled samples in both PE180 and PE360 (24% and 50% smaller than PC180 and PC360, respectively, see Table A1), which is similar to the observed deterioration in the peak load at 180 cycles, but much higher than that observed at 360 cycles.

Fig. 6c and d also present the peak load, and the debonding energy of the glass-based TRMs reinforced with "single yarn+ transverse elements" as reported in [35], where the specimens (named as GT) were cured and exposed to a similar FT condition. Like single glass yarn, the peak load and debonding energy of GT specimens under FT conditions increase up to 180 cycles and then decrease until the end of the test. The peak load of GT yarns is in the same range as single yarns, but their debonding energy is higher due to the effects of transverse elements. This shows that the presence of transverse yarns does not affect the deterioration rates in the bidirectional fabric studied here.

The bond-slip laws of the samples are derived using stress-based analytical modeling from the experimental load-slip curves. The model assumes that displacements and tractions continue at the interface and embedded length. In addition, the adhesive and frictional bonds are assumed to govern sliding at the bonded and debonded lengths, respectively. Therefore, the pull-out bond shear strength (τ_{max}) and the frictional shear strength (τ_f) are the key parameters of the bond-slip laws. The readers are referred to [60,61] for the detailed discussions and formulations for calculating these parameters. Fig. 6e and f present the changes in the bond-slip law parameters under the control and FT conditions. Also, Table A 1 reports the average of those parameters for each test series. It can be observed that the τ_{max} and τ_f increase 106% and 9%, respectively, in the controlled samples until 180 days of exposure (PC180) and then decrease resting at a total decrement of 44% and 27% with respect to PC0 or 73% and 33% with respect to PC180 samples. These values are comparable to those obtained from FT exposed specimens, again, showing the FT exposure did not govern the deterioration mechanisms in these samples. A similar trend can also be observed in the bond and frictional strength of the samples with transverse yarns, $\tau_{max,GT}$ and $\tau_{f,GT}$, but overall those values are slightly higher than the ones obtained from the samples without transverse yarns.

3.3 TRM tensile behavior

Fig. 7a shows the typical tensile stress-strain response and cracking pattern of TRMs at 0 cycles and their experimental average (of five samples). In addition, Fig. 7b presents the average stress-strain curves of the specimens at 0, 180, and 360 cycles under both control and exposed conditions. The experimental load is divided by the cross-section area of the yarns (2.645 mm^2) to calculate the stress. The strain equals the mean displacements from the two LVDTs divided by their base length (310 mm). A set of parallel and horizontal cracks followed by rupturing yarns are the governing failure mode in all the specimens under the control and the FT conditions, as shown in Fig. 7a. The linear, the crack development, and the post-cracking stages of the tensile response are identified in the tensile-strain curves (Fig. 7a).

Stress (σ), as the tensile response parameter, of individual specimens is reported together with a linear regression line showing the general trend of the experimental results in Fig. 7c and d (details given in Table A 2). In Fig. 7c and d, the stresses associated with the transition points from linear to crack development, and from crack development to post-cracking stages of the tensile behavior (named σ_1 and σ_2, respectively). Under FT cycles, the σ_1 and σ_2 increase up to 180 cycles and then decrease until the end of the tests. In contrast, σ_1 does not change and σ_2 decreases in the control specimens during the same period. After 180 cycles, the σ_1 and σ_2 of exposed specimens decrease until the test end, while those of control specimens do not change significantly. As a result, σ_1 and σ_2 are 25% and 51% higher in exposed specimens at 180 cycles (TE180) compared to control samples at the same age (TC180). In contrast, these values are 43% and 9% less in TE360 samples compared to TC360. The observed changes in the tensile stress at the linear stage (σ_1) under both conditions are in line with the evolution of the flexural strength of the mortar M1. In the crack development stage, only frictional stresses are available between yarns and mortar, due to cracking and weakening of the bond at the interface of yarn-to-mortar [62]. Consequently, changes in σ_2 are consistent to changes in frictional shear strength (τ_f) of yarn-to-mortar bond (presented in previous section). Besides, the crack spacing for both control and exposed specimens shows a slightly increasing trend, as shown in Fig. 7e.

3.4 TRM-to-substrate bond behavior

Fig. 8a reports the typical load-slip curves of the individual TRM-to-substrate specimens and their experimental average at 0 cycles. Additionally, Fig. 8b presents the average load-slip curves of the specimens at 0, 180, and 360 cycles under both control and exposed conditions. The curves are the average of five specimens, and the load in these curves is divided by the number of yarns (3 yarns). The control samples fail because of yarns slippage, while exposed samples fail due to either yarns slippage or yarns slippage followed by tensile rupture (see Table A 3). It should be noted that no debonding has occurred at the TRM-to-substrate interface in any of the specimens due to the enhancement of the bond as a result of sandblasting of the brick's surfaces. Also, the similar CTE of the brick and the mortar M1 ensured that the stresses developed at the mortar-to-brick interface are not high to cause interfacial cracking during the FT cycles.

The single-lap shear peak load changes under both conditions are presented in Fig. 8c with a linear regression trending line for better understanding (see Table A 3 for the exact values). As shown in Fig. 8c, the peak load changes under the FT condition are slightly increasing up to 180 cycles, in contrast, the control specimens show a slightly decreasing trend during this period. Up to the end of the test, both the control and the exposed specimens show a considerable decreasing trend, like the yarn-to-mortar bond behavior. Therefore, this deterioration can be attributed to other parameters such as mortar age effect or mortar shrinkage. The results of these conditions need to be explored further in future research. Furthermore, the quantitative comparison between the FT and control conditions shows that the peak loads of SE180 and SE360 specimens (exposed specimens after 180- and 360-FT cycles) are respectively 30% and 8% higher than those of SC180 and SC360 (control specimens after 180 and 360T cycles).

Fig. 8d also shows the average peak stress of the pull-out ($\sigma_{pull\text{-}out}$) and the single-lap ($\sigma_{single\text{-}lap}$) specimens compared to the average tensile stress of the TRM composite at the end of the linear

(σ_1) and the crack development stages (σ_2) under the FT conditions. As shown, $\sigma_{pull\text{-}out}$ and $\sigma_{single\text{-}lap}$ are close to the σ_1, indicating the bond strength of the whole system decreases before cracks appear in the mortar samples. However, in some points (240 and 300 cycles), $\sigma_{single\text{-}lap}$ is close to the σ_2 due to fiber rupturing in these samples. Moreover, comparison of $\sigma_{pull\text{-}out}$ and $\sigma_{single\text{-}lap}$ shows that these two stresses are equal up to 120 cycles, but after this point, $\sigma_{pull\text{-}out}$ is less than $\sigma_{single\text{-}lap}$. This can be attributed to the fact that the bond degradation effect on mesh fabric is less than that on single yarns [39]. In addition, it is important to take into account that the bond length of pull-out specimens varies from those of single-lap specimens (50 mm versus 100 mm, respectively).

3.5 In-plane behavior

Sliding along the mortar joint is the most common failure mode for unreinforced panels (UD), both for control and FT conditioned specimens. In a small number of cases, sliding along the mortar joint is combined with cracking in the masonry units, as presented in Table 3 and Fig. 9. As for the strengthened panels (SD), the failure occurred under both conditions: formation of two diagonal cracks in the center of the TRM composite, tensile failure of yarns, followed by developing diagonal cracks. Besides, there is no debonding between the TRM composite and the substrate under any conditions, as expected from the single-lap shear tests results.

The average load-displacement (vertical and horizontal LVDT measurements) response of the unreinforced and strengthened panels is presented in Fig. 9a and b. Also, Fig. 9c shows the average shear stress-strain curve of each series calculated according to ASTM- E 519-2 [57].

Furthermore, the main characteristics values of the in-plane response are summarized in Table 3, including the maximum load (P_{max}), the maximum shear stress (τ'_{max}) and its corresponding strain (γ_{max}), the pseudo-ductility ratio ($\mu_{diagonal} = \gamma_u / \gamma_y$), and the shear modulus (G). γ_u is the ultimate shear strain corresponding to a 20 % strength drop on the post-peak softening branch of the shear stress-strain curve, and γ_y is the shear strain at 75 % of the maximum shear stress [29,63,64]. γ_u of UD panels is equal to γ_{max} due to bearing load until the peak load. G is computed by the secant modulus between 5% and 30% of the maximum shear stress [29].

Compared with unreinforced panels at zero cycle (UDC0), UDC360 and UDE360 panels show a significant decrement of τ'_{max} (70% and 62%, respectively) and shear modulus, G (93% and 82%, respectively). Whereas γ_{max} of UDC360 and UDE360 increases considerably by 157% and 86%

compared to UDC0, and $\mu_{diagonal}$ stays almost constant, as presented in Table 3. These results contrast with the changes observed in the mechanical properties of the brick and the mortar M2 under both conditions. This shows the importance of the mortar-to-brick bond (at the bed and head joints) deterioration, which was not experimentally measured in this study and is proposed for future investigations. Additionally, the transportation of the panels from the chamber to the testing site may also have affected their in-plane behavior; however, this could be occurring for both control and exposed samples, hence its effect is expected to be seen in all the results. Also, a visual inspection revealed no cracks.

In strengthened panels, no significant changes occurred in all in-plane parameters under both conditions (SDC360 and SDE360), compared to the reinforced panels at zero cycles (SDC0), as listed in Table 3. The in-plane parameters show that the FT conditions slightly improve P_{max} and G by 13% and 10%, in SDE360 samples compared to the control ones at the same age (SDC360). However, γ_u and $\mu_{diagonal}$, parameters related to the post-peak area, slightly decrease under FT (16% and 15%, respectively).

3.6 Out-of-plane behavior

Fig. 10 illustrates the load-displacement curves and failures of the bending tests. All unreinforced panels (UP and UN) show a brittle behavior and fail suddenly by reaching the peak load under the control and FT conditions. A single crack crossing the panel develops in both the UP and UN specimens, except that it occurs along the bed joint in the UP panels (Fig. 10a). However, a crack occurs around the units in alternate courses in the UN panels, as presented in Fig. 10c. Strengthened panels (SP and SN) fail suddenly by reaching load to the tensile strength of the glass fabrics at the constant moment region under the control and the FT conditions. Two wide cracks occur in the TRM composite of SP panels, and then panels fail at the masonry bed joint like the UP panels, as presented in Fig. 10b. One wide crack causes SN panels to fail through the masonry units (Fig. 10d), contrasting with the failure of unreinforced panels (UN series). Additionally, no TRM-to-masonry detachment is observed in any strengthened panels under the control and the FT conditions. 113 mm, 135 mm, and 125 mm are the average crack spacing for SPC0, SPC360, and SPE360, respectively, which is slightly different from the crack spacing observed in the TRM tensile tests. This difference can be due to the different load application and boundary conditions in these two test methods.

Table 4 and Table 5 present the cracking and maximum loads (P_{cr}, P_{max}), their corresponding deflection (Δ_{cr}, Δ_{max}), maximum bending (M_{max}) at the mid-span, ductility ($\mu_{bending}$), and orthogonal strength ratio (OSR), as the main characteristics values of the out-of-plane response. $\mu_{bending}$ is defined as follows [29]:

$$\mu_{bending} = \frac{1}{2}\left(\frac{E_{max}}{E_{cr}} + 1\right) \quad (1)$$

where E_{max} and E_{cr} are the areas under the load-displacement curve until P_{max} and P_{cr}, respectively. Also, orthogonal strength ratio (OSR) is defined as the gross area modulus of rupture (R) of UP or SP panels to that of UN or SN panels, respectively, and shows the anisotropy degree of masonry [65]:

$$OSR = \frac{R_P}{R_N}, R_{P\ or\ N} = \frac{\left(P_{max} + 0.75P_s\right)L_s}{b_m t^2} \quad (2)$$

L_s is the outer span length (420 mm), b_m is the width of the panels (420 mm for UP and SP panels, and 330 mm for UN and SN panels), and t is the thickness of the panels (100 mm). P_s is the self-weight of panels equal to zero due to testing specimens in the vertical position.

According to Table 4 and Table 5, all out-of-plane parameters of unreinforced panels (for both failure parallel (UP) and normal (UN) to bed joints) decline under the control and the FT conditions, compared to the panels at zero cycles. For example, P_{max}, M_{max}, and E_{max} of UPE360 (FT exposed panels) specimens decrease by 17%, 11%, and 36%, compared to panels at zero cycles (UPC0). These values drop by 40%, 44%, and 47%, respectively, for UPC360 (control panels). A similar decreasing trend can be observed for the UNE360 (P_{max}:26%, M_{max}:27%, and E_{max}:47%) and UNC360 (P_{max}:48%, M_{max}:49%, and E_{max}:11%) panels, compared to UNC0 panels. These observations contrast with the changes in the mechanical properties of the brick and the mortar M2 under both conditions. An influential factor in reducing out-of-plane response can be weakening the bond (at the bed and head joints) between the brick and mortar. Furthermore, comparing the results of UPE360 with UPC360 reveals that the proposed FT conditions cause the out-of-plane parameters (P_{max}, M_{max}, and E_{max}) to improve by 38%, 60%, and 21%, respectively. For UNE360 panels, P_{max} and M_{max} improve by 42% and 44% compared to UNC360 panels. It can result from promoting mortar hydration in high humidity conditions present at the proposed FT cycles (90% RH).

The changes of the out-of-plane parameters in the strengthened panels (for both failure parallel (SP) and normal (SN) to bed joints) are different from those of unreinforced panels, as presented in Table 4 and Table 5. Compared to zero cycles, P_{max}, M_{max}, and E_{max} of all strengthened panels decrease under the control and the FT conditions. For instance, these parameters decrease for SPE360 (FT exposed panels) by 22%, 22%, and 4% and for SPC360 panels by 24%, 26%, and 13%, respectively. Also, SNE360 panels show decrement of P_{max}, M_{max}, and E_{max} by 22%, 21%, and 13%, while only P_{max} and M_{max} of SNC360 panels decrease by 22% and 19%. This reduction in the out-of-plane response can be the result of the observed reduction of the tensile strength in the TRM composites (as discussed in section 3.3) and the reduction in the flexural strength of masonry (as discussed in the previous paragraphs) under both conditions. However, other parameters (E_{cr}, $\mu_{debonding}$, and OSR) do not exhibit a specific trend of increasing or decreasing. Furthermore, comparing the results of strengthened panels in the last stage of the experiment (SPE360 vs. SPC360, and SNE360 vs. SNC360) shows no significant difference between the out-of-plane parameters of control and exposed specimens.

4 Analytical modeling

4.1 Prediction of tensile crack spacing of TRM composite

Through the ACK (Aveston–Cooper–Kelly) theory, the saturation crack spacing (X) can be predicted in tensile specimens. Based on this theory, it is assumed that the yarns are only capable of carrying load along their longitudinal axis, and when mortar cracks and debonds from the textile, a constant frictional stress replaces the previously existing adhesion stress. By imposing the equilibrium force along the loading axes of the yarns [62,66], one obtains:

$$X = 1.337 \frac{\upsilon_m r \sigma_{mu}}{\upsilon_f 2\tau_f} \quad (3)$$

where υ_f is the volumetric fractions of the yarns calculated as the ratio between the yarn area mesh and the average cross-section of the tensile specimens (υ_f= 0.00335), and υ_m is the volumetric fractions of the mortar equal to 1-υ_f [29]. r is the yarn radius and equal to 0.5298 mm [29] by considering a circular section area for the yarns. τ_f is the frictional shear strength at the yarn-to-mortar interface obtained from the pull-out tests (Table A 1). σ_{mu} refers to the mortar's direct tensile strength and can be derived from the compressive (f_m), flexural (f_{fl}), or splitting (f_{sp}) strengths

[29,67]. Fig. 11 presents the X value for 0, 180, and 360 cycles compared with the upper and lower limit of experimental crack spacing under FT conditions. In Fig. 11, X_{PE} and X_{GT} are the predicted crack spacing based on the frictional shear strength (τ_f) of "single yarn" and "single + transverse yarn" bond, respectively. Also, Table A 4 presents the formulations and values for predicting X_{PE} and X_{GT} at zero cycles. It can be observed from Fig. 11 that the expected crack spacing for each cycle is between upper and lower experimental values and is predicted with an acceptable degree of accuracy. However, the crack spacing values predicted by tensile splitting strength and single yarn (X_{PE}-f_{sp}) at 180 and 360 FT cycles are a little higher than the experimental results. In general, the experimental average results at zero, 180, and 360-FT cycles are well predicted by the combination of flexural strength and single yarn (X_{PE}-f_{fl}).

4.2 Prediction of compressive strength of masonry prism

The formulation presented by Eurocode 6 [68] can be used here to compute the compressive strength of masonry prisms ($f'_{masonry}$). Therefore, the compressive strength of masonry made with general purpose mortar is:

$$f'_{masonry} = K f_b^{\alpha} f_m^{\beta} \quad (4)$$

where K is a constant to be defined and modified, which is equal to 0.55 for clay brick. f_b and f_m are the compressive strength of the brick and the mortar M2, respectively, as presented in Table 2. α and β are constant related to the f_b and f_m and equal to 0.7 and 0.3. $f'_{masonry}$ can be found as 9.6 MPa, 9.3 MPa, and 9.6 MPa for C0, C360, and E360 cycles, respectively, showing 14%, 8%, and 1% error with respect to the experimental results. Besides constants (K, α, and β), the change in mortar strength over time also impacts the results. As an example, in control samples (C0 and C360) with the same brick strength, mortar strength after 120 days and 367 days is 8.7 and 7.8, respectively, causing an error of 14% and 8%.

4.3 Prediction of panels shear strength

As the unreinforced panels (UDC0, UDC360, and UDE360) failed due to sliding along the mortar joint, their shear strength (V_m) can be estimated as follows [29,69]:

$$V_m = \frac{\tau_0}{1-\mu_0 \tan\theta} A_n, \ \theta = 45^{\circ} \quad (5)$$

τ_0 represents the shear bond strength equal to 0.26 MPa (at 28 days) as reported in another study conducted by the authors [29]. The coefficient of internal shear friction (μ_0) in mortar joints is also considered to be 0.4 based on Eurocode 6 [68]. A_n is the net area of the specimen and equals to 54000 mm^2. Therefore, V_m is equal to 23.4 kN, a value that is 43% lower than the experimental result of UDC0, and 80% and 35% higher than those of UDC360 and UDE360 (Table 3), respectively. The difference can be explained by considering constant values for the τ_0 and μ_0. Eurocode 6 [68] proposes τ_0 based on the compressive strength of mortar (f_m) and it is equivalent to 0.2 MPa at C0 and C360 and to 0.3 MPa at E360. Using these values in Eq. (5), the V_m compared to UDC0 is 56% lower, and to UDC360 and UDE360 it is 38% and 53% higher, respectively. Besides, μ_0 can be varied between 0.3 and 1.2 [70], therefore if considering μ_0= 0.74 and τ_0= 0.2 at C0, V_m will match to 41.5 kN with 1% error to UDC0. If μ_0= 0.3 and τ_0= 0.2 at C360, V_m will be equal to 15.4 kN showing 18% error to UDC360. Finally, by considering both μ_0 and τ_0 equal to 0.3 at E360, V_m will be 23 kN showing 30% error to UDE360.

TRM-reinforced panels have a nominal shear capacity (V_n) derived from the masonry (V_m) and the TRM composites (V_f), as reported in ACI 549.6R-20 [71]. Due to the diagonal tension failure of strengthened panels, the following equation can be used to calculate the V_m:

$$V_m = \frac{\tan\theta + \sqrt{21.16 + \tan^2\theta}}{10.58} f_t' A_n \left(\frac{L}{H_w}\right), f_t' = 0.67\sqrt{f_{masonry}} \quad \text{...} \quad (6)$$

where f'_t is the tensile strength of masonry, L is the panel's length (540 mm), H_w is the panel's height (540 mm), and $f_{masonry}$ is the compressive strength of masonry prism (Table 2). V_m for the SDC0, SDC360, and SDE360 is equal to 65 kN, 62 kN, and 61 kN, respectively, showing higher value than the experimental results of unreinforced panels (UDC0, UDC360, UDE360).

The TRM composite applied to both sides of the panel provides the following shear capacity (V_f) [29,71]:

$$V_f = 2\left(nA_f L E_f \varepsilon_{fd}\right) \quad \text{...} \quad (7)$$

where n is the number of fabric layers (n= 1), and A_f is the fabric area per unit width in both directions (0.07054 mm^2/mm). E_f is the tensile modulus of elasticity of cracked TRM (E_3 from Table A 2) and ε_{fd} is the design value of the strain of TRM composites under direct tensile. ACI 549.6R-20 [71] suggests ε_{fd} is the average value of the tensile experimental results (ε_3 from Table A 2) minus one standard deviation. Table 6 lists the values of ε_{fd}, V_f, and the proportion of

V_n to the maximum experimental load under the control and the FT conditions. The results show error of 23%~43% compared to the experimental results. The difference between analytical and experimental results is partly due to the use of the design value of strain (ε_{fd}). The error would decrease to 19%~34% if the ultimate tensile experimental results (ε_3) were used in Eq. (7). Furthermore, the different performance of TRM composites at the micro (TRM tensile test) and masonry panel levels lead the error to increase.

4.4 Prediction of panels flexural strength

The Eurocode 6 [68] estimates the formula for calculating the nominal flexural strength of unreinforced masonry panels (M_{Rd}):

$$M_{Rd} = S\,f_{xk} \quad (8)$$

where S is the section modulus of un-crack wallets equal to 7×10^5 mm^3 and 5.5×10^5 mm^3 for UP and UN panels. f_{xk} is the flexural strength of masonry and is 0.15 MPa and 0.4 MPa for UP and UN panels, based on [68]. Therefore, M_{Rd} of UP panels is equal to 0.105 kN.m, which is higher than the experimental results of UPC0, UPC360, and UPE360 by 17%, 110%, and 31% (Table 4), respectively. M_{Rd} of UN panels is 0.22 kN.m, which is lower than that of the experimental results (UNC0, UNC360, and UNE360) by 65%, 31%, and 52%, respectively (Table 5). The difference can be attributed to the estimated flexural strength of the masonry (f_{xk}), especially over the long term.

The nominal flexural strength (M_n) of TRM-strengthened panels is calculated as follows [71]:

$$M_n = \left(c\,\gamma\,f_{masonry}\,\beta_1\,b_m\right)\left(\frac{t}{2} - \frac{\beta_1}{2}c\right) + \left(E_f\,\varepsilon_{fd}\,A'_f\,b_m\right)\frac{t}{2} \quad (9)$$

$$\beta_1 = \gamma = 0.7$$

where A'_f is the fabric area per unit width (0.03572 mm^2/mm), and c is the neutral axis depth which is calculated as follows:

$$c = \frac{A'_f\,E_f\,\varepsilon_{fd}}{\gamma\,\beta_1 f_{masonry}} \quad (10)$$

The values of $f_{masonry}$ and E_f can be found in Table 2 and Table A 2 for C0, C360, and E360 cycles. According to ACI 549.6R-20 [71], the design tensile strength (ε_{fd}) is the minimum of the ultimate tensile strain of TRM composite (ε_3 from Table A 2) and 0.012. Table 6 lists the nominal flexural strength and its proportion to the experimental results. The results show an error of 57~68% error for the ACI 549.6R-20 [71] method. This observation also agrees with the findings of other studies [72–74].

5 Conclusions

An extensive experimental campaign was presented in this study to investigate the durability of TRM composites under freeze-thaw conditions. The TRM composite considered is made of an AR-glass fabric embedded in a hydraulic lime-based mortar. A series of multi-level experimental tests were performed to investigate the potential effects of freeze-thaw conditions on the mechanical performance of these composites and TRM-strengthened masonry components at the micro-, meso-, and macro-scales. The following key conclusions can be drawn based on the obtained results:

- The FT conditions marginally enhanced the mechanical properties of the mortar M1, similar to the control specimens. The mortar hydration continued until the end of the tests (360 cycles or 337 days) and caused the FT conditions to have fewer adverse effects. This could result from the sample saturation not being adequate, despite 90% RH exposure conditions. A similar observation was made for the mortar M2, indicating that the FT conditions' detrimental effect was less than their effect on promoting the mortar hydration. Additionally, the FT conditions did not affect considerably the mechanical properties of the brick and the glass fabric, as expected.
- The yarn-to-mortar bond behavior deteriorated under 180-FT cycles in a way comparable to the control specimens in a similar age. However, as the test progressed, both the control and exposed samples showed a decreasing trend, indicating more destructive effects of other parameters (e.g., reduction of elastic modulus of mortar M1) on the bond response than the proposed FT conditions. In addition, a similar observation was observed for the bond-slip law parameters (bond shear strength, τ_{max}, and frictional stress, τ_f).
- The tensile behavior of the TRM composite under FT conditions improved up to 180 cycles, compared to the control specimens. In contrast, when the number of FT cycles was increased up to 360, the tensile behavior degraded. Additionally, the results demonstrated that the tensile behavior of the TRM composites was in agreement with the flexural behavior of mortar M1 at the linear stage and the frictional stress of yarn-to-mortar at the crack development stage.

- For the single-lap shear specimens under FT conditions, the peak load changes improved up to 180 cycles compared with the control specimens. As the test progressed, both control and exposed specimens displayed a decreasing trend in the same way, proving that FT conditions had no effect on TRM-to-substrate bond. When compared to the pull-out test, the single-lap shear test revealed that the bond degradation effect on mesh fabric was less than that on single yarns.
- Under both conditions and the test end, the yarn-to-mortar bond response, the TRM tensile strength, and the TRM-to-substrate bond properties of the glass-based TRM composite were significantly declined, while the strength of reinforced panels remained relatively unchanged. Therefore, it is imperative to investigate the durability of these composites at different scales.
- The in-plane and out-of-plane behavior of the URM panels declined under both control and the FT conditions due to the bond degradation at the bed and head joints. In contrast, the in-plane and out-of-plane behavior of strengthened panels did not change significantly.
- By using ACK theory and pull-out test results, crack spacing was predicted reasonably well in tensile test samples under both the control and FT conditions.
- The mechanical properties of the masonry were predicted. The results showed that the compressive strength of the masonry could be predicted (by Eurocode 6 [68]) with high accuracy under both conditions.
- The in-plane and out-of-plane capacity of strengthened panels was predicted analytically based on ACI 549.6R-20 [71]. Results showed considerable differences between the analytical and experimental results due to different TRM composite performance at multi-levels.

Consequently, using 90% RH exposure conditions was not adequate, especially at the material and the masonry panel level, so that a higher saturation level was recommended. In addition, by the end of the tests (360 cycles or 337 days), other factors (e.g., mortar age effect or shrinkage) appeared to affect severely the fabric-to-mortar interface at the micro- and meso-level, compared to the proposed FT conditions. Future research should examine the results of these factors.

6 Acknowledgments

This work was partly financed by FCT/MCTES through national funds (PIDDAC) under the R&D Unit Institute for Sustainability and Innovation in Structural Engineering (ISISE), under reference UIDB/04029/2020. The support to the first author through grant agreement SFRH/BD/131282/2017, provided by FCT- Foundation for Science and Technology, is kindly acknowledged.

7 References

[1] M.R. Valluzzi, V. Modena, Claudio, G. de Felice, Current practice and open issues in strengthening historical buildings with composites, Mater. Struct. 47 (2014) 1971–1985. https://doi.org/10.1617/s11527-014-0359-7.

[2] M. Angelillo, ed., Mechanics of masonry structures, 2014. https://doi.org/10.1007/978-3-7091-1774-3.

[3] Z.A. Al-Jaberi, J.J. Myers, M.A. EIGawady, Evaluation of FRP and FRCM composites for the strengthening of reinforced masonry walls, Am. Concr. Institute, ACI Spec. Publ. 2017-Octob (2017) 513–528. https://doi.org/10.14359/51713353.

[4] E. Mustafaraj, Y. Yardim, Retrofitting damaged unreinforced masonry using external shear strengthening techniques, J. Build. Eng. 26 (2019) 100913. https://doi.org/10.1016/j.jobe.2019.100913.

[5] A.S. Mosallam, Out-of-plane flexural behavior of unreinforced red brick walls strengthened with FRP composites, Compos. Part B Eng. 38 (2007) 559–574. https://doi.org/10.1016/j.compositesb.2006.07.019.

[6] T.L. Bui, A. Si Larbi, N. Reboul, E. Ferrier, Shear behavior of masonry walls strengthened by external bonded FRP and TRC, Compos. Struct. 132 (2015) 923–932. https://doi.org/10.1016/j.compstruct.2015.06.057.

[7] A. Jafari, A. Vatani Oskouei, M. Bazli, R. Ghahri, Effect of the FRP sheet’s arrays and NSM FRP bars on in-plane behavior of URM walls, J. Build. Eng. 20 (2018) 679–695. https://doi.org/10.1016/j.jobe.2018.09.018.

[8] J. Lanas, J.L. Perez Bernal, M.A. Bello, J.I. Alvarez, Mechanical properties of masonry repair dolomitic lime-based mortars, Cem. Concr. Res. 36 (2006) 951–960. https://doi.org/10.1016/j.cemconres.2005.10.004.

[9] C.G. Papanicolaou, T.C. Triantafillou, M. Papathanasiou, K. Karlos, Textile reinforced mortar (TRM) versus FRP as strengthening material of URM walls: out-of-plane cyclic loading, Mater. Struct. 41 (2007) 143–157. https://doi.org/10.1617/s11527-007-9226-0.

[10] C.G. Papanicolaou, T.C. Triantafillou, M. Papathanasiou, K. Karlos, Textile-reinforced mortar (TRM) versus FRP as strengthening material of URM walls: in-plane cyclic loading, Mater. Struct. 40 (2007) 1081–1097. https://doi.org/10.1617/s11527-006-9207-8.

[11] G. de Felice, S. De Santis, L. Garmendia, P. Larrinaga, P.B. Lourenço, D. V Oliveira, C.G. Papanicolaou, Mortar-based systems for externally bonded strengthening of masonry, Mater. Struct. 47 (2014) 2021–2037. https://doi.org/10.1617/s11527-014-0360-1.

[12] S.M. Raoof, L.N. Koutas, D.A. Bournas, Textile-reinforced mortar (TRM) versus fibre-reinforced polymers (FRP) in flexural strengthening of RC beams, Constr. Build. Mater. 151 (2017) 279–291. https://doi.org/10.1016/j.conbuildmat.2017.05.023.

[13] A. Dalalbashi, B. Ghiassi, D.V. Oliveira, A. Freitas, Fiber-to-mortar bond behavior in TRM composites: effect of embedded length and fiber configuration, Compos. Part B Eng. 152 (2018) 43–57. https://doi.org/10.1016/j.compositesb.2018.06.014.

[14] J. Jiang, C. Jiang, B. Li, P. Feng, Bond behavior of basalt textile meshes in ultra-high ductility cementitious composites, Compos. Part B Eng. 174 (2019) 107022. https://doi.org/10.1016/j.compositesb.2019.107022.

[15] A. Dalalbashi, B. Ghiassi, D. V. Oliveira, Textile-to-mortar bond behaviour in lime-based textile reinforced mortars, Constr. Build. Mater. 227 (2019) 116682. https://doi.org/10.1016/j.conbuildmat.2019.116682.

[16] A. Younis, U. Ebead, Bond characteristics of different FRCM systems, Constr. Build. Mater. 175 (2018) 610–620. https://doi.org/10.1016/j.conbuildmat.2018.04.216.

[17] M. Leone, M.A. Aiello, A. Balsamo, F.G. Carozzi, F. Ceroni, M. Corradi, M. Gams, E. Garbin, N. Gattesco, P. Krajewski, C. Mazzotti, D. Oliveira, C. Papanicolaou, G. Ranocchiai, F. Roscini, D. Saenger, Glass fabric reinforced cementitious matrix: Tensile properties and bond performance on masonry substrate, Compos. Part B Eng. 127 (2017). https://doi.org/10.1016/j.compositesb.2017.06.028.

[18] C. Sabau, J.H. Gonzalez-Libreros, L.H. Sneed, G. Sas, C. Pellegrino, B. Täljsten, Use of image correlation system to study the bond behavior of FRCM-concrete joints, Mater. Struct. 50 (2017). https://doi.org/10.1617/s11527-017-1036-4.

[19] C. Pellegrino, J. Sena-Cruz, eds., Design procedures for the use of composites in strengthening of reinforced concrete structures- State-of-the-Art report of the RILEM technical committee 234-DUC, RILEM, Springer, 2016. https://doi.org/10.1007/978-94-017-7336-2 ISSN.
[20] B. Ghiassi, D. V Oliveira, V. Marques, E. Soares, H. Maljaee, Multi-level characterization of steel reinforced mortars for strengthening of masonry structures, Mater. Des. 110 (2016) 903–913. https://doi.org/10.1016/j.matdes.2016.08.034.
[21] C. Signorini, A. Nobili, E.I. Cedillo González, C. Siligardi, Silica coating for interphase bond enhancement of carbon and AR-glass Textile Reinforced Mortar (TRM), Compos. Part B Eng. 141 (2018) 191–202. https://doi.org/10.1016/j.compositesb.2017.12.045.
[22] C. Chiu, X. Wang, Z. Zhang, Y. Zhu, Experimental and numerical investigations of the tensile behaviour of steel-TRM prepared with recycled glass sands and lime, Constr. Build. Mater. 280 (2021) 122512. https://doi.org/10.1016/j.conbuildmat.2021.122512.
[23] Y. Yao, F.A. Silva, M. Butler, V. Mechtcherine, B. Mobasher, Tension stiffening in textile-reinforced concrete under high speed tensile loads, Cem. Concr. Compos. 64 (2015). https://doi.org/10.1016/j.cemconcomp.2015.07.009.
[24] F. Ferretti, C. Mazzotti, FRCM/SRG strengthened masonry in diagonal compression: experimental results and analytical approach proposal, Constr. Build. Mater. 283 (2021) 122766. https://doi.org/10.1016/j.conbuildmat.2021.122766.
[25] C. Papanicolaou, T. Triantafillou, M. Lekka, Externally bonded grids as strengthening and seismic retrofitting materials of masonry panels, Constr. Build. Mater. 25 (2011) 504–514. https://doi.org/10.1016/j.conbuildmat.2010.07.018.
[26] L. Mercedes, E. Bernat-Maso, L. Gil, In-plane cyclic loading of masonry walls strengthened by vegetal-fabric-reinforced cementitious matrix (FRCM) composites, Eng. Struct. 221 (2020) 111097. https://doi.org/10.1016/j.engstruct.2020.111097.
[27] M. Angiolilli, A. Gregori, M. Pathirage, G. Cusatis, Fiber Reinforced Cementitious Matrix (FRCM) for strengthening historical stone masonry structures: Experiments and computations, Eng. Struct. 224 (2020) 111102. https://doi.org/10.1016/j.engstruct.2020.111102.
[28] S. Türkmen, B.T. De Vries, S.N.M. Wijte, A.T. Vermeltfoort, In-plane behaviour of clay brick masonry wallettes retrofitted with single-sided fabric-reinforced cementitious matrix

and deep mounted carbon fibre strips, Springer Netherlands, 2020. https://doi.org/10.1007/s10518-019-00596-2.
[29] A. Dalalbashi, B. Ghiassi, D. V. Oliveira, A multi-level investigation on the mechanical response of TRM-strengthened masonry, Mater. Struct. 54 (2022). https://doi.org/10.1617/s11527-021-01817-4.
[30] L. Garcia-Ramonda, L. Pelà, P. Roca, G. Camata, Cyclic shear-compression testing of brick masonry walls repaired and retrofitted with basalt textile reinforced mortar, Compos. Struct. (2021) 115068. https://doi.org/10.1016/j.compstruct.2021.115068.
[31] C. D'Ambra, G.P. Lignola, A. Prota, F. Fabbrocino, E. Sacco, FRCM strengthening of clay brick walls for out of plane loads, Compos. Part B Eng. 174 (2019) 107050. https://doi.org/10.1016/j.compositesb.2019.107050.
[32] E. Bernat-Maso, C. Escrig, C.A. Aranha, L. Gil, Experimental assessment of Textile Reinforced Sprayed Mortar strengthening system for brickwork wallettes, Constr. Build. Mater. 50 (2014) 226–236. https://doi.org/10.1016/j.conbuildmat.2013.09.031.
[33] B. Ghiassi, Mechanics and durability of textile reinforced mortars: a review of recent advances and open issues, RILEM Tech. Lett. 4 (2019) 130–137. https://doi.org/10.21809/rilemtechlett.2019.99.
[34] M. Alma'aitah, B. Ghiassi, A. Dalalbashi, Durability of textile reinforced concrete: Existing knowledge and current gaps, Appl. Sci. 11 (2021) 1–10. https://doi.org/10.3390/app11062771.
[35] A. Nobili, Durability assessment of impregnated Glass Fabric Reinforced Cementitious Matrix (GFRCM) composites in the alkaline and saline environments, Constr. Build. Mater. 105 (2016) 465–471. https://doi.org/10.1016/j.conbuildmat.2015.12.173.
[36] F. Ceroni, A. Bonati, V. Galimberti, A. Occhiuzzi, Effects of environmental conditioning on the bond behavior of FRP and FRCM systems applied to concrete elements, J. Eng. Mech. 144 (2018) 04017144. https://doi.org/10.1061/(ASCE)EM.1943-7889.0001375.
[37] M. Uranjek, V. Bokan-bosiljkov, Influence of freeze – thaw cycles on mechanical properties of historical brick masonry, Constr. Build. Mater. 84 (2015) 416–428. https://doi.org/10.1016/j.conbuildmat.2015.03.077.
[38] A. Dalalbashi, B. Ghiassi, D. V. Oliveira, Aging of lime-based TRM composites under natural environmental conditions, Constr. Build. Mater. 270 (2021).

https://doi.org/10.1016/j.conbuildmat.2020.121853.

[39] A. Dalalbashi, B. Ghiassi, D.V. Oliveira, Influence of freeze-thaw cycles on the pull-out response of lime-based TRM composites, Constr. Build. Mater. 313 (2021). https://doi.org/10.1016/j.conbuildmat.2021.125473.

[40] A. Dalalbashi, B. Ghiassi, D. V. Oliveira, Freeze-thaw durability of glass textile-reinforced mortar composites, in: 17th Int. Brick Block Mason. Conf. (IBMAC 2020), Taylor & Francis Group, Kraków, 2020. https://doi.org/10.1201/9781003098508-152.

[41] I.G. Colombo, M. Colombo, M. Prisco, Tensile behavior of textile reinforced concrete subjected to freezing-thawing cycles in un-cracked and cracked regimes, Cem. Concr. Res. 73 (2015) 169–183. https://doi.org/10.1016/j.cemconres.2015.03.001.

[42] B.Y. Pekmezci, E. Arabaci, C. Ustundag, Freeze-thaw durability of lime based FRCM systems for strengthening historical masonry, Key Eng. Mater. 817 KEM (2019) 174–181. https://doi.org/10.4028/www.scientific.net/KEM.817.174.

[43] M. De Munck, M. El Kadi, E. Tsangouri, J. Vervloet, S. Verbruggen, J. Wastiels, T. Tysmans, O. Remy, Influence of environmental loading on the tensile and cracking behaviour of textile reinforced cementitious composites, Constr. Build. Mater. 181 (2018). https://doi.org/10.1016/j.conbuildmat.2018.06.045.

[44] A. Nobili, C. Signorini, On the effect of curing time and environmental exposure on impregnated Carbon Fabric Reinforced Cementitious Matrix (CFRCM) composite with design considerations, Compos. Part B. 112 (2017) 300–313. https://doi.org/10.1016/j.compositesb.2016.12.022.

[45] J. Donnini, F. Bompadre, V. Corinaldesi, Tensile behavior of a glass FRCM system after different environmental exposures, Processes. 8 (2020). https://doi.org/10.3390/pr8091074.

[46] Z.K. Al-jaberi, J.J. Myers, Effect of long-term environmental exposure on EB-FRP or FRCM-reinforced masonry system, in: G. Milani, A. Taliercio, S. Garrity (Eds.), 10th Int. Mason. Conf., Milan, 2018.

[47] H. Maljaee, B. Ghiassi, P.B. Lourenço, D. V Oliveira, FRP- brick masonry bond degradation under hygrothermal conditions, Compos. Struct. 147 (2016) 143–154. https://doi.org/10.1016/j.compstruct.2016.03.037.

[48] ASTM C109/C109M-05, Standard test method for compressive strength of hydraulic cement mortars (Using 2-in. or [50-mm] Cube Specimens), 2005.

https://doi.org/10.1520/C0109_C0109M-05.

[49] BS EN 1015-11, Methods of test for mortar for masonry. Determination of flexural and compressive strength of hardened mortar, 1999.

[50] BS EN 12390-13, Testing hardened concrete. Determination of secant modulus of elasticity in compression, 2013.

[51] ASTM C496/C496M- 04, Standard test method for splitting tensile strength of cylindrical concrete specimens, 2004. https://doi.org/10.1520/C0496_C0496M-04.

[52] ASTM C67-05, Standard test methods for smpling and testing brick and structural clay tile, 2005. https://doi.org/10.1520/C0067_C0067M-20.

[53] EN 772-1. Methods of test for masonry units – Part 1: Determination of compressive strength, 2000.

[54] ASTM C1314-03, Standard test method for compressive strength of masonry prisms, 2003. https://doi.org/10.1520/C1314-18.

[55] A. Dalalbashi, B. Ghiassi, D.V. Oliveira, A. Freitas, Effect of test setup on the fiber-to-mortar pull-out response in TRM composites: experimental and analytical modeling, Compos. Part B Eng. 143 (2018) 250–268. https://doi.org/10.1016/j.compositesb.2018.02.010.

[56] A. Dalalbashi, S. De Santis, B. Ghiassi, D. V. Oliveira, Slip rate effects and cyclic behaviour of textile-to-matrix bond in textile reinforced mortar composites, Mater. Struct. 54 (2021). https://doi.org/10.1617/s11527-021-01706-w.

[57] ASTM E519-02, Standard test method for diagonal tension (shear) in masonry assemblages, 2002. https://doi.org/10.1520/E0519-02.

[58] BS EN 1052-2, Methods of test for masonry- Part2: Determination of flexural strength., 1999.

[59] B. Ghiassi, D. V Oliveira, P.B. Lourenço, Hygrothermal durability of bond in FRP-strengthened masonry, (2014) 2039–2050. https://doi.org/10.1617/s11527-014-0375-7.

[60] A. Dalalbashi, B. Ghiassi, D. V. Oliveira, Textile-to-mortar bond behavior: An analytical study, Constr. Build. Mater. 282 (2021) 122639. https://doi.org/10.1016/j.conbuildmat.2021.122639.

[61] A. Dalalbashi, B. Ghiassi, D. V. Oliveira, Analytical modeling of the bond behavior between textile and mortar based on pull-out tests, Key Eng. Mater. 817 (2019) 112–117.

https://doi.org/10.4028/www.scientific.net/KEM.817.112.

[62] H. Cuypers, J. Wastiels, Stochastic matrix-cracking model for textile reinforced cementitious composites under tensile loading, Mater. Struct. 39 (2006) 777–786. https://doi.org/10.1617/s11527-005-9053-0.

[63] X. Wang, C.C. Lam, V.P. Iu, Experimental investigation of in-plane shear behaviour of grey clay brick masonry panels strengthened with SRG, Eng. Struct. 162 (2018) 84–96. https://doi.org/10.1016/j.engstruct.2018.02.027.

[64] F. Parisi, I. Iovinella, A. Balsamo, N. Augenti, A. Prota, In-plane behaviour of tuff masonry strengthened with inorganic matrix–grid composites, Compos. Part B Eng. 45 (2013). https://doi.org/10.1016/j.compositesb.2012.09.068.

[65] ASTM E518-02, Standard test method for flexural bond strength of masonry, 2003. https://doi.org/10.1520/E0518-03.

[66] J. Aveston, G. Cooper, A. Kelly, Single and multiple fracture, the properties of fibre composites., in: Proc. Conf. Natl. Phys. Lab., London: IPC Science and Technology Press Ltd., 1971: pp. 15–24.

[67] fib- International Federation for Structural Concrete. fib Model Code for Concrete Structures 2010, 2013. https://doi.org/10.1002/9783433604090.

[68] European Committee for Standardization, EN 1996-1-1: Design of masonry structures - Part 1-1: General rules for reinforced and unreinforced masonry structures, 2018.

[69] ACI Committee 440, ACI 440.7R-10 Guide for design and construction of externally bonded FRP systems for strengthening unreinforced masonry structures, 2010.

[70] T. Paulay, M.J.N. Priestely, Seismic design of reinforced concrete and masonry buildings, Wiley Interscience, 1992.

[71] ACI Committee 549, ACI 549.6R-20 Guide to design and construction of externally bonded fabric-reinforced cementitious matrix (FRCM) and steel-reinforced grout (SRG) systems for repair and strengthening masonry structures, 2020.

[72] S.L. Sagar, V. Singhal, D.C. Rai, P. Gudur, Diagonal Shear and Out-of-Plane Flexural Strength of Fabric-Reinforced Cementitious Matrix–Strengthened Masonry Walletes, J. Compos. Constr. 21 (2017). https://doi.org/10.1061/(ASCE)CC.1943-5614.0000796.

[73] S. Babaeidarabad, D. Arboleda, G. Loreto, A. Nanni, Shear strengthening of un-reinforced concrete masonry walls with fabric-reinforced-cementitious-matrix, Constr. Build. Mater.

65 (2014) 243–253. https://doi.org/10.1016/j.conbuildmat.2014.04.116.

[74] T. D'Antino, F.G. Carozzi, P. Colombi, C. Poggi, Out-of-plane maximum resisting bending moment of masonry walls strengthened with FRCM composites, Compos. Struct. 202 (2018) 881–896. https://doi.org/10.1016/j.compstruct.2018.04.054.

8 List of tables

Table 1. Experimental program.

Task	Material	Control specimens corresponding to FT exposures cycles			Freeze-Thaw (FT) cycles						Name	Total number of specimens
		C0	C180	C360	E60	E120	E180	E240	E300	E360		
Compressive test	M1	5	5	5	5	5	5	5	5	5	-	45
	M2	5	5	5	-	-	5	-	-	5	-	25
	Brick	5	-	5	-	-	-	-	-	5	-	15
	Masonry prism	5	-	5	-	-	-	-	-	5	-	15
Flexural test	M1	5	5	5	-	-	5	-	-	5	-	25
	M2	5	-	5	-	-	-	-	-	5	-	15
	Brick	5	-	5	-	-	-	-	-	5	-	15
Determination of elastic modulus	M1	5	5	5	-	-	5	-	-	5	-	25
	M2	5	-	5	-	-	-	-	-	5	-	15
	Brick	5	-	5	-	-	-	-	-	5	-	15
Splitting test	M1	5	5	5	-	-	5	-	-	5	-	25
	M2	5	-	5	-	-	-	-	-	5	-	15
Tensile test	Glass fiber	5	-	5	-	-	-	-	-	5	-	15
	TRM composite	5	5	5	5	5	5	5	5	5	TC0, TC180, TC360, TE60~ TE360	45
Pull-out test	yarn-to-mortar bond	5	5	5	5	5	5	5	5	5	PC0, PC180, PC360, PE60~ PE360	45
Single-lap shear test	TRM-to-substrate	5	5	5	5	5	5	5	5	5	SC0, SC180, SC360, SE60~ SE360	45
Diagonal compression test	URM panel	4	-	4	-	-	-	-	-	4	UDC0, UDC360, UDE360	12
	Strengthened panel	4	-	4	-	-	-	-	-	4	SDC0, SDC360, SDE360	12
Bending test (failure parallel to bed joint)	URM panel	4	-	4	-	-	-	-	-	4	UPC0, UPC360, UPE360	12
	Strengthened panel	4	-	4	-	-	-	-	-	4	SPC0, SPC360, SPE360	12
Bending test (failure normal to bed joint)	URM panel	4	-	4	-	-	-	-	-	4	UNC0, UNC360, UNE360	12
	Strengthened panel	4	-	4	-	-	-	-	-	4	SNC0, SNC360, SNE360	12

Table 2. Mechanical properties of the mortars and the brick. *

Property [MPa]	Material	Control specimens [cycles]			Exposed specimens [cycles]					
		C0	C180	C360	E60	E120	E180	E240	E300	E360
Compressive strength	M1	16.8 (11)	20 (12)	17.3 (10)	17.0 (10)	19.0 (22)	19.5 (5)	17.5 (4)	17.3 (2)	18.8 (3)
	M2	8.7 (6)	6.0 (9)	7.8 (4)	-	-	8.3 (6)	-	-	9.8 (5)
	Brick	23.5 (5)	-	-	-	-	-	-	-	22.5 (7)
	Masonry prism	11.1 (8)	-	10.1 (17)	-	-	-	-	-	9.7 (13)
Flexural strength	M1	4.5 (2)	4.5 (12)	4.7 (5)	-	-	5.8 (5)	-	-	5.0 (5)
	M2	1.7 (9)	-	1.4 (7)	-	-	-	-	-	1.6 (7)
	Brick	4.5 (14)	-	-	-	-	-	-	-	4.5 (6)
Elastic modulus	M1	6713 (6)	8280 (11)	8095 (10)	-	-	7593 (1)	-	-	7462 (12)
	M2	5236 (10)	-	3301 (8)	-	-	-	-	-	4875 (13)
	Brick	9650 (2)	-	-	-	-	-	-	-	9476 (2)
	Glass fiber (warp)	65940 (5)	-	-	-	-	-	-	-	70720 (3)
	Glass fiber (weft)	69870 (4)	-	-	-	-	-	-	-	72910 (3)
Splitting strength	M1	1.4 (8)	2.0 (14)	2.1 (8)	-	-	2.2 (3)	-	-	2.2 (9)
	M2	0.5 (7)	-	0.6 (15)	-	-	-	-	-	0.6 (17)
Tensile strength	Glass fiber (warp)	875 (13)	-	-	-	-	-	-	-	899 (5)
	Glass fiber (weft)	685 (9)	-	-	-	-	-	-	-	676 (12)

*CoV of the results is given in percentage inside parentheses.

Table 3. Diagonal compression test results. *

Name	P_{max} [kN]	Failure	τ'_{max} [MPa]	γ_{max} [%]	γ_y [%]	γ_u [%]	$\mu_{diagonal}$	G [MPa]
UDC0	41.04 (22)	A & B	0.60 (31)	0.07 (47)	0.04 (40)	0.07 (47)	1.97 (13)	1815 (76)
UDC360	13.01 (14)	B	0.18 (14)	0.18 (9)	0.11 (6)	0.18 (9)	1.58 (5)	129 (19)
UDE360	17.64 (30)	B	0.23 (17)	0.13 (15)	0.06 (26)	0.13 (15)	2.12 (14)	320 (31)
SDC0	151.01 (0)	D & C	1.80 (1)	0.11 (5)	0.07 (2)	0.24 (1)	3.44 (3)	2035 (1)
SDC360	148.54 (2)	D & C	1.83 (3)	0.11 (15)	0.06 (3)	0.25 (6)	3.90 (6)	2186 (8)
SDE360	168.48 (4)	D & C	1.92 (6)	0.11 (11)	0.06 (9)	0.21 (24)	3.30 (19)	2398 (8)

*CoV of the results is given in percentage inside parentheses.
A: combined sliding along mortar joint and cracking in the masonry units; B: sliding along mortar joint; C: cracking in the masonry units; D: TRM failure.

Table 4. Bending test results: failure parallel to bed joints. *

Name	Δ_{cr} [mm]	P_{cr} [kN]	Δ_{max} [mm]	P_{max} [kN]	M_{max} [kN.m]	E_{cr} [kN.mm]	E_{max} [kN.mm]	$\mu_{bending}$	R [N/mm^2]	OSR
UPC0	-	-	1.05 (37)	1.5 (34)	0.09 (34)	-	1 (50)	-	0.15 (34)	9.50
UPC360	-	-	0.91 (34)	0.9 (21)	0.05 (21)	-	0.53 (46)	-	0.09 (21)	7.7
UPE360	-	-	0.76 (26)	1.24 (15)	0.08 (15)	-	0.64 (41)	-	0.12 (15)	7.64
SPC0	0.36 (1)	22 (10)	2.81 (3)	41 (1)	2.58 (1)	5 (11)	82 (9)	9 (2)	4.13 (1)	0.97
SPC360	0.52 (9)	21 (10)	3.38 (8)	31 (9)	1.91 (9)	6 (22)	71 (14)	6.50 (16)	3.06 (9)	1.06
SPE360	0.35 (29)	21 (9)	3.32 (13)	32 (5)	2.01 (5)	4.03 (28)	78.73 (12)	11.66 (42)	3.21 (5)	0.98

*CoV of the results is given in percentage inside parentheses.

Table 5. Bending test results: failure normal to bed joints. *

Cycles	Δ_{cr} [mm]	P_{cr} [kN]	Δ_{max} [mm]	P_{max} [kN]	M_{max} [kN.m]	E_{cr} [kN.mm]	E_{max} [kN.mm]	$\mu_{bending}$	R [N/mm^2]
UNC0	-	-	0.26 (51)	10 (21)	0.63 (21)	-	1.9 (72)	-	1.42 (33)
UNC0	-	-	0.42 (26)	5.2 (2)	0.32 (2)	-	1.7 (25)	-	0.66 (2)
UNE360	-	-	0.18 (25)	7.4 (10)	0.46 (10)	-	1.0 (24)	-	0.95 (10)
SNC0	0.18 (13)	28 (13)	1.83 (8)	32 (23)	1.97 (23)	3 (29)	46 (15)	8 (16)	4.01 (23)
SNC360	0.24 (16)	24 (5)	2.18 (8)	25 (7)	1.59 (7)	4.12 (14)	46.04 (8)	6.18 (13)	3.24 (7)
SNE360	0.20 (27)	26 (7)	1.83 (8)	25 (8)	1.55 (8)	3 (20)	40 (13)	6.48 (23)	3.15 (8)

*CoV of the results is given in percentage inside parentheses.

Table 6. Prediction of the nominal shear and flexural strength capacity of TRM-strengthened panels based on ACI 549.6R-20 [71].

In-plane	ε_{fd} [%]			V_f [kN]			V_n/P_{max} [%]		
	SDC0	SDC360	SDE360	SDC0	SDC360	SDE360	SDC0	SDC360	SDE360
	1.077	0.55	1.31	51.4	22.4	47.5	77	57	64
Out-of-plane	ε_{fd} [%]			M_n [kN.mm]			M_n/M_{max} [%]		
failure parallel to bed joint	SPC0	SPC360	SPE360	SPC0	SPC360	SPE360	SPC0	SPC360	SPE360
	1.19	0.82	1.2	1.09	0.64	0.83	42	34	41
failure normal to bed joint	SNC0	SNC360	SNE360	SNC0	SNC360	SNE360	SNC0	SNC360	SNE360
	1.19	0.82	1.2	0.85	0.51	0.65	43	32	42

9 List of figures

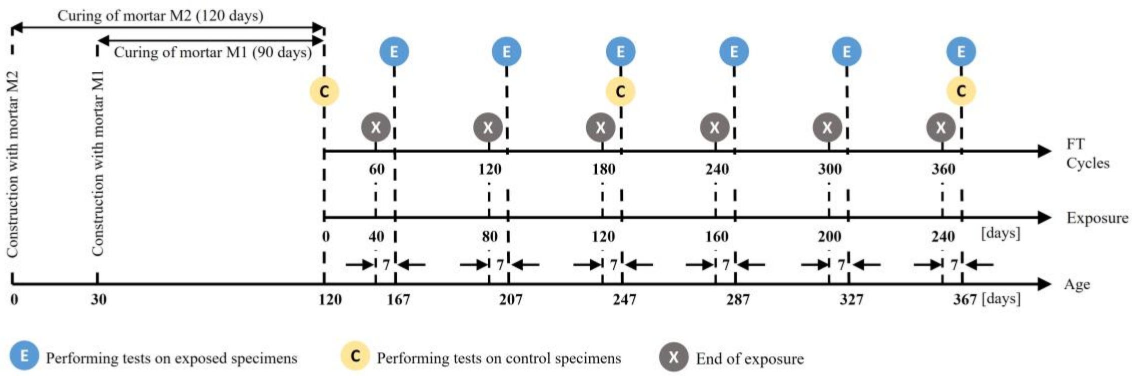

Fig. 1. Schematic representation of the test program.

Fig. 2. Material characterization: (a) AR-glass fabric (b) cube compressive test; (c) prism flexural test; (d) splitting test; (e) cylinder elastic modulus test; (f) prism elastic modulus test; (g) masonry prism compressive test; (h) fiber tensile test.

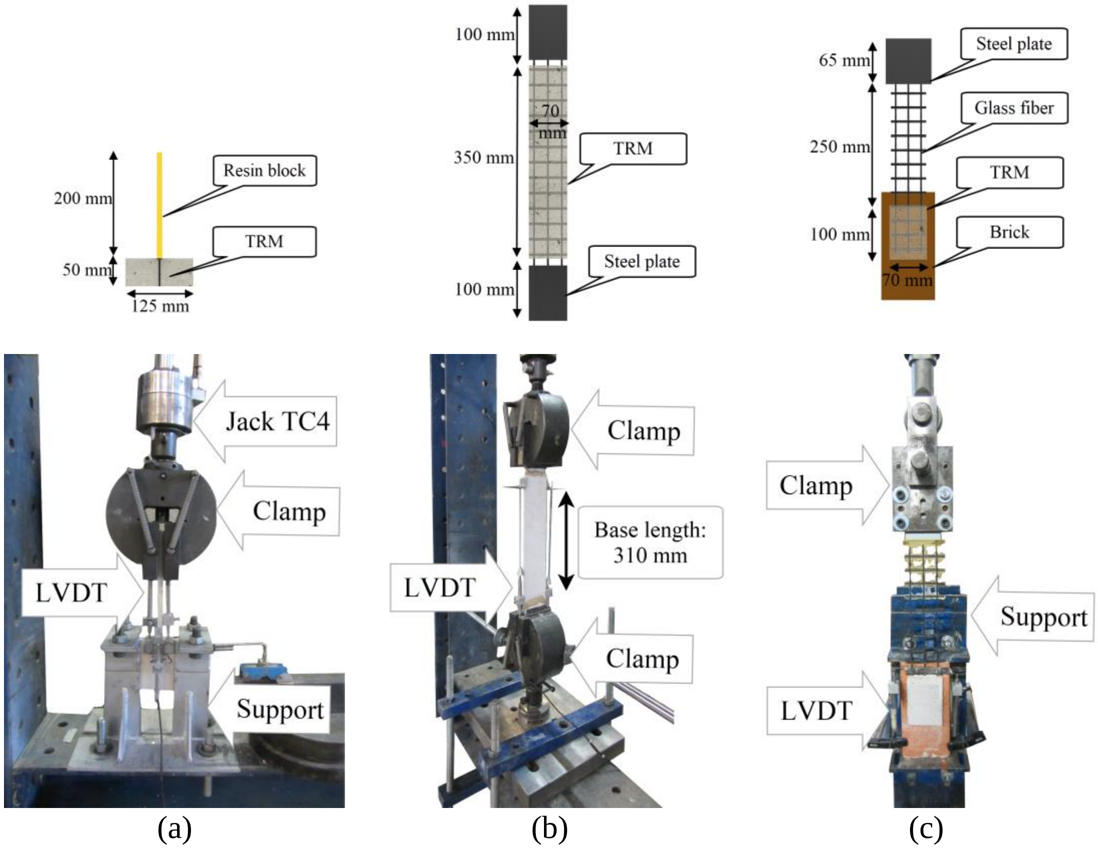

Fig. 3. Geometrical details and test setups: (a) pull-out test; (b) tensile test; (c) single-lap shear test.

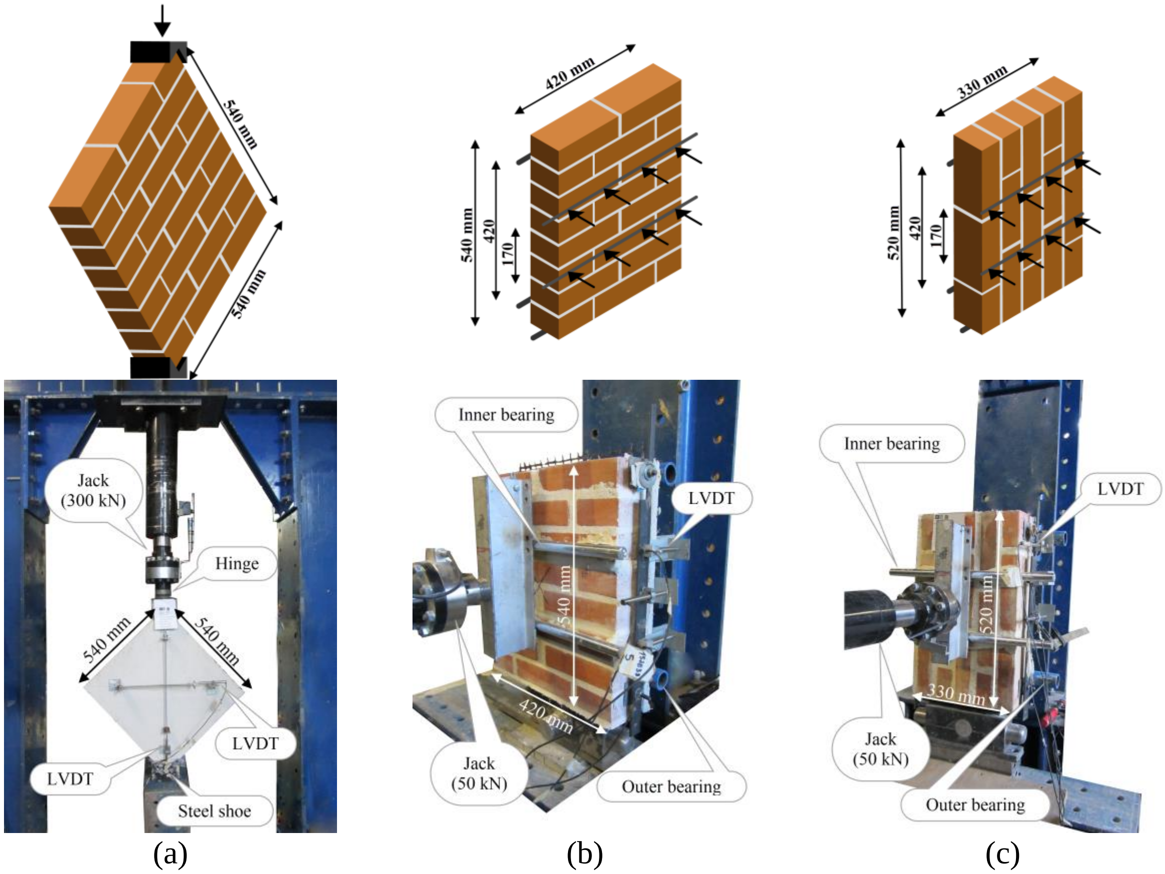

Fig. 4. Geometric details and test setups used for testing masonry panels: (a) diagonal compression tests; (b) bending tests parallel to bed joint; (c) bending tests normal to bed joints.

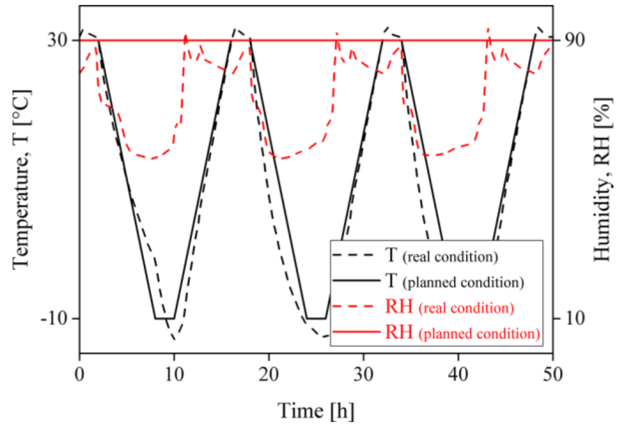

Fig. 5. Freeze-thaw cycles.

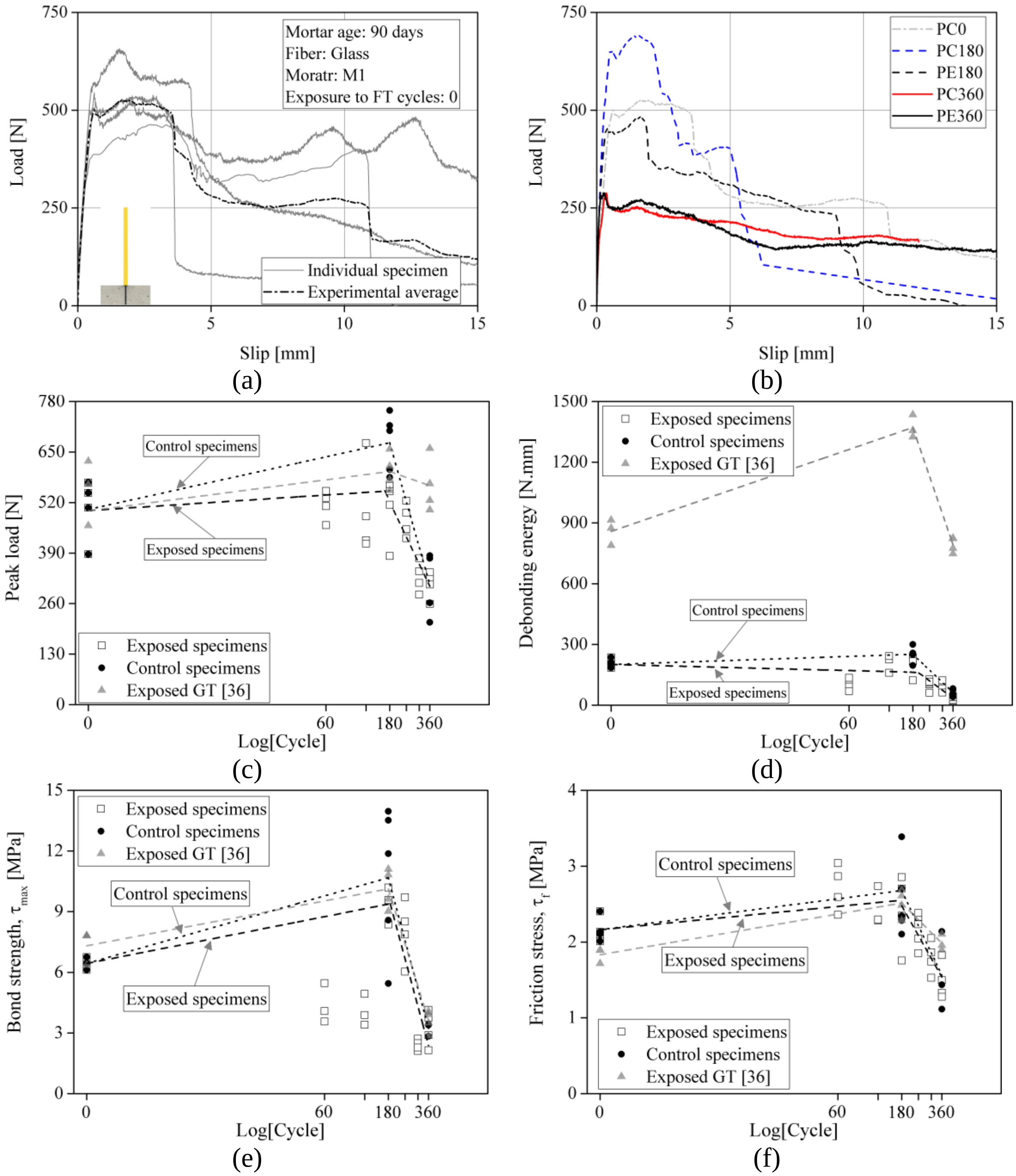

Fig. 6. Pull-out response: (a) typical pull-out behavior of individual samples; (b) the average load-slip curves of exposed and control specimens at 0, 180, and 360 cycles; (c) peak load; (d) debonding energy; (e) bond shear strength; (f) friction stress.

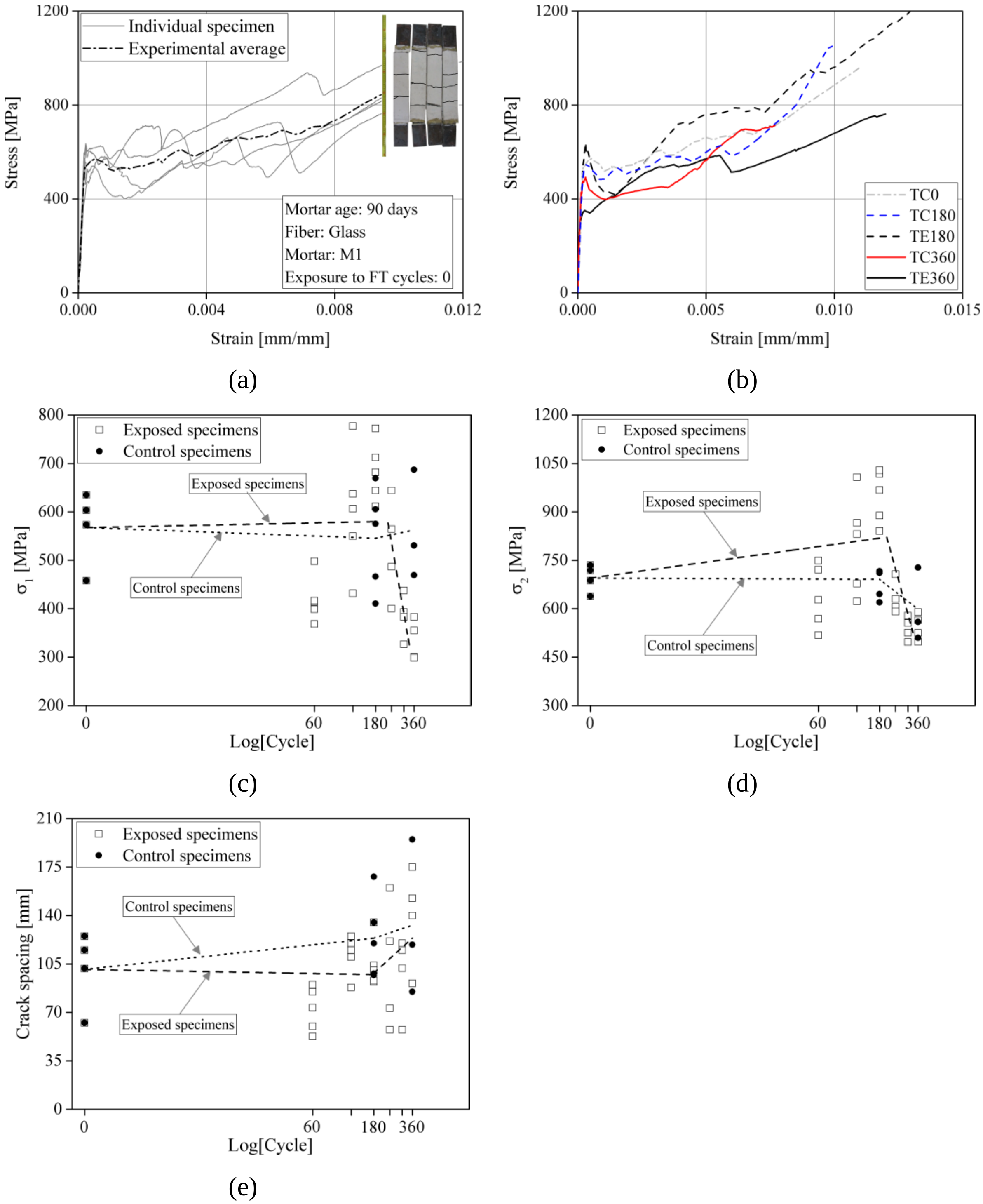

Fig. 7. TRM composite tensile response: (a) typical tensile behavior of individual samples; (b) the average stress-strain curves of exposed and control specimens at 0, 180, and 360 cycles; (c) stress of linear stage; (d) stress of crack development stage; (e) crack spacing.

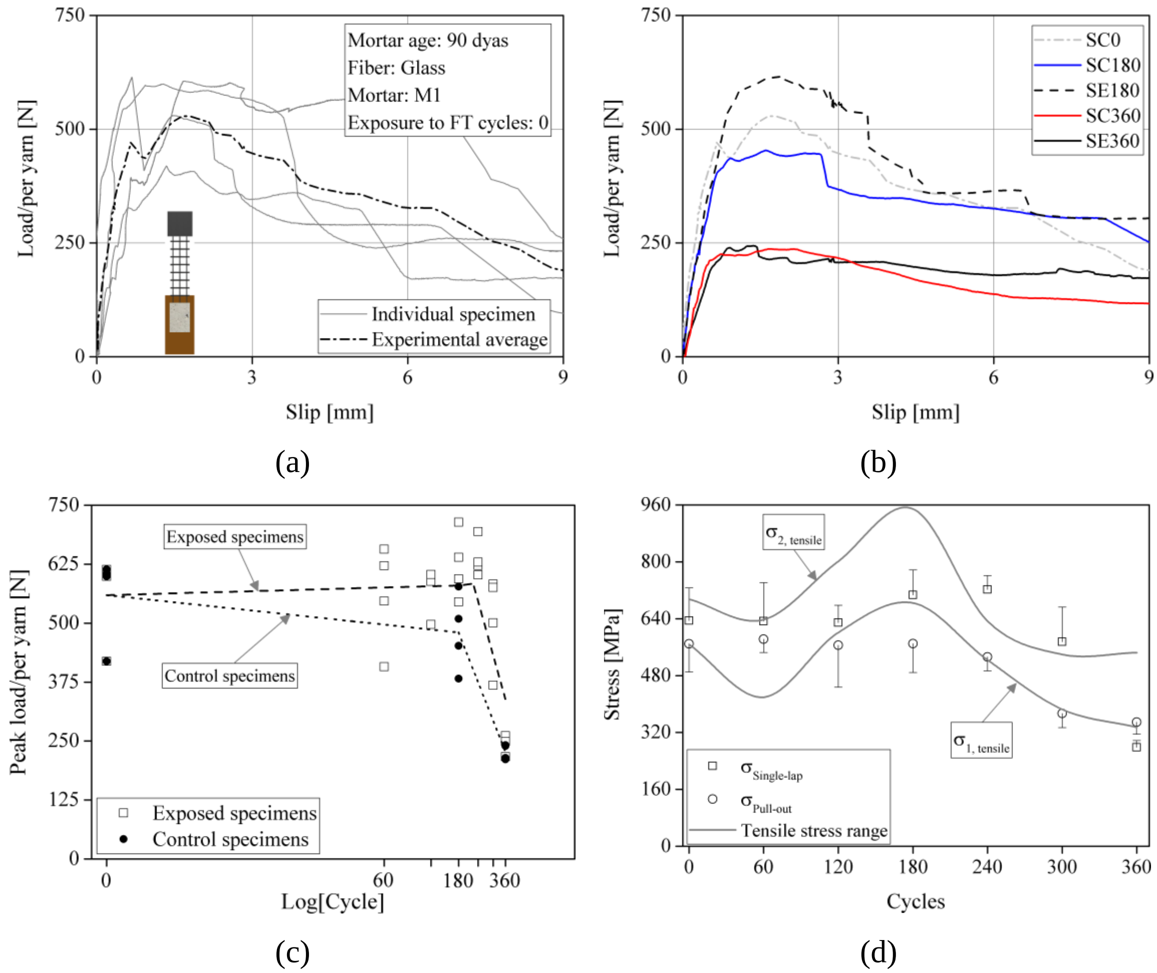

Fig. 8. TRM-to-substrate response: (a) typical load-slip curve of individual samples; (c) peak load changes; (d) average stress at the exposed bond level specimens.

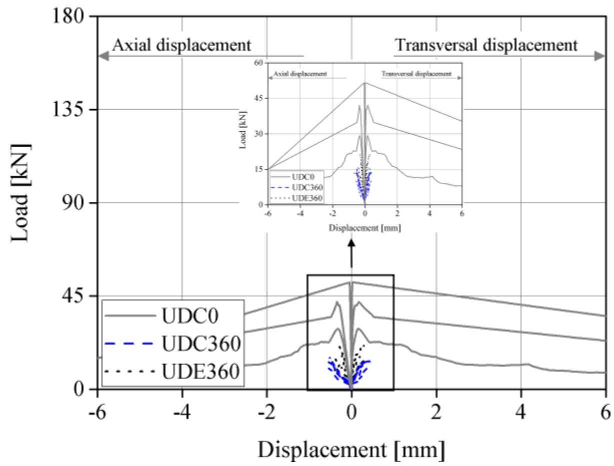

(a)

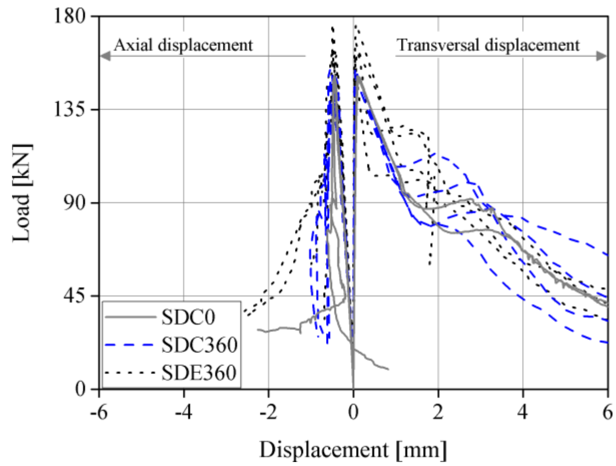

(b)

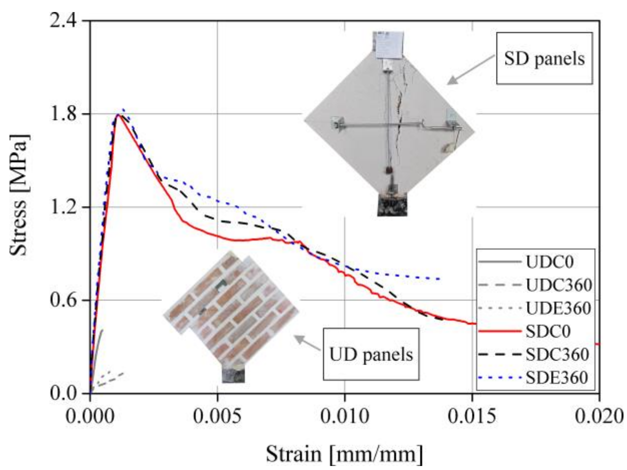

(c)

Fig. 9. Diagonal compression result: (a, b) load-displacement curves of URM and strengthened-masonry panels; (c) average shear stress-strain curves.

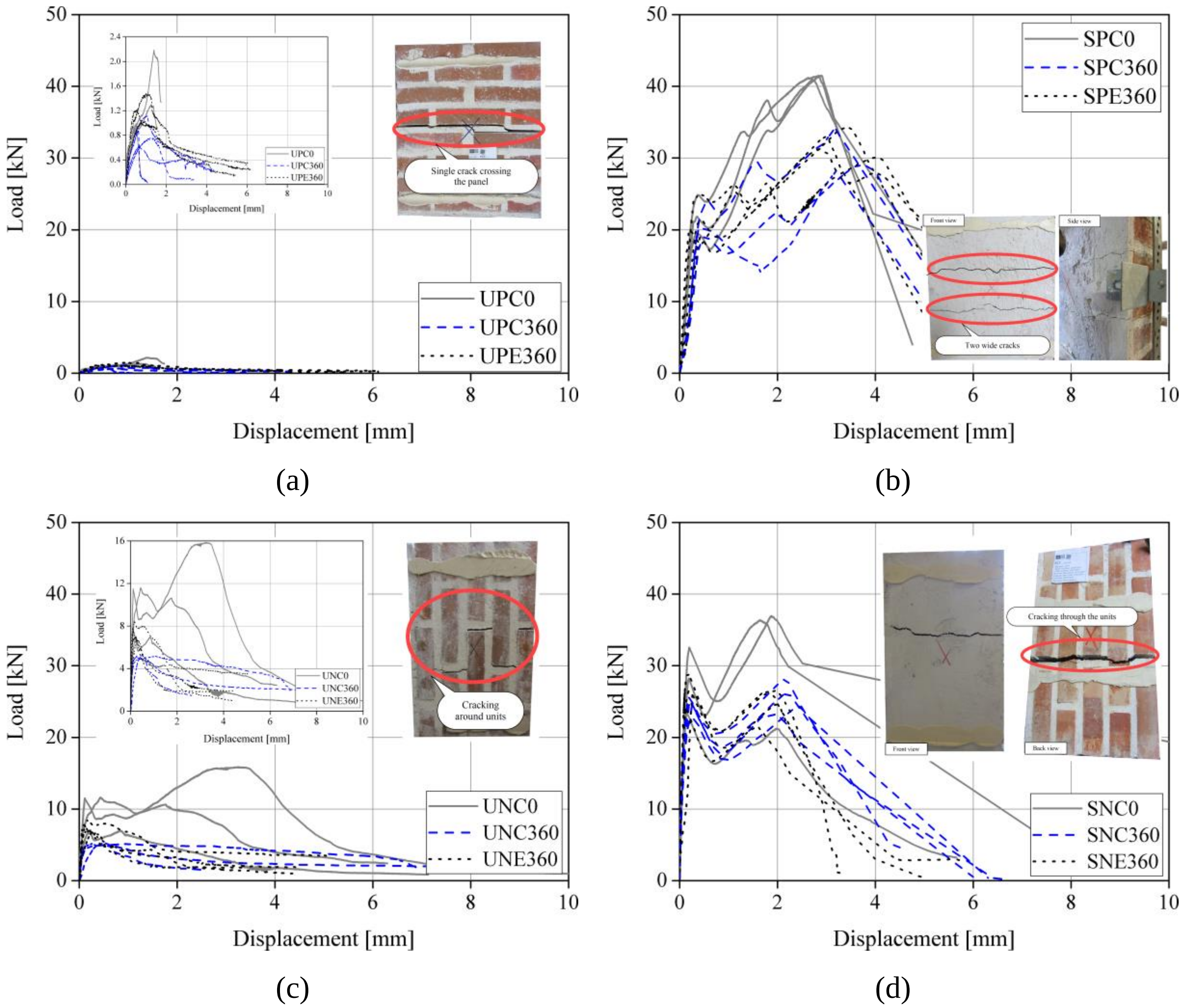

Fig. 10. Load-displacement curves of bending tests: (a, b) failure parallel to bed joint of un-strengthened and strengthened panels; (c, d) failure normal to bed joint of un-strengthened and strengthened panels.

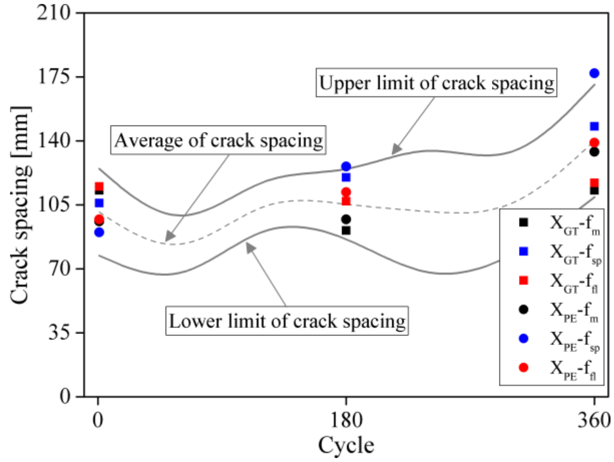

Fig. 11. Comparing crack spacing of experimental tensile tests and ACK model under FT conditions.

10 Appendix

Table A 1. Pull-out properties of TRM composite. *

Name	P_P [N]	E_{deb} [N.mm]	τ_{max} [MPa]	τ_f [MPa]	$\tau_{max,GT}$ [MPa]	$\tau_{f,GT}$ [MPa]
PC0	502.3 (14)	208.1 (9)	5.8 (19)	2.2 (7)	7.3 (9)	1.8 (5)
PC180	673.9 (10)	251.6 (13)	12 (18)	2.4 (9)	-	-
PC360	308.4 (24)	63.3 (25)	3.2 (8)	1.6 (27)	3.7 (28)	2 (19)
PE60	513.5 (6)	105.6 (25)	4.4 (18)	2.7 (11)	-	-
PE120	498.7 (21)	208.9 (17)	4.1 (16)	2.4 (9)	-	-
PE180	502.4 (14)	191.4 (26)	9.4 (8)	2.4 (18)	-	-
PE240	469.6 (7)	103.3 (22)	8 (17)	2.2 (9)	-	-
PE300	329.2 (11)	90.6 (24)	2.4 (9)	1.8 (11)	-	-
PE360	308.0 (10)	31.5 (15)	3.2 (24)	1.7 (10)	3.6 (13)	2 (4)

*Coefficients of variation in percentage terms are provided inside parentheses.
P_P: peak load; E_{deb}: debonding energy; τ_{max}: bond shear strength; τ_f: friction stress; $\tau_{max,GT}$ and $\tau_{f,GT}$ are related to the "single + transverse" yarn.

Table A 2. TRM tensile behavior. *

Name	σ_1 [MPa]	σ_2 [MPa]	E_3 [GPa]	ε_3 [%]	Number of cracks	Distance between cracks [mm]
TC0	567.5 (12)	695 (5)	62.7 (15)	1.19 (9)	3 (13)	101 (23)
TC180	545.5 (17)	673.1 (6)	83.4 (13)	1.09 (15)	2 (32)	124 (21)
TC360	562.4 (16)	598.9 (16)	53.5 (21)	0.82 (32)	2 (28)	133 (35)
TE60	419.2 (10)	637 (14)	59.1 (12)	1.66 (10)	4 (23)	72 (20)
TE120	600.5 (19)	801.1 (17)	63.7 (20)	1.21 (9)	2 (20)	112 (11)
TE180	684.3 (8)	948.8 (8)	69.6 (12)	1.2 (10)	2 (18)	105 (15)
TE240	524 (17)	633.4 (7)	70.0 (9)	0.91 (24)	2 (19)	101 (39)
TE300	385.1 (10)	539.3 (6)	51.4 (22)	1.39 (18)	3 (0)	99 (25)
TE360	334.3 (11)	544.2 (7)	47.6 (17)	1.51 (13)	2 (25)	140 (22)

*Coefficients of variation in percentage terms are provided inside parentheses.
1, 2, and 3 are related to the linear, the crack development, and the post-cracking stages of TRM tensile behavior.

Table A 3. TRM-to-substrate bond properties. *

Name	Peak load/per yarn [N]	Failure
SC0	559.4 (15)	Yarns slippage
SC180	480.2 (15)	Yarns slippage
SC360	226.6 (6)	Yarns slippage
SE60	558.1 (17)	Yarns slippage
SE120	554.9 (8)	Yarns slippage followed by rupturing
SE180	623.1 (10)	Yarns slippage followed by rupturing
SE240	636.9 (5)	Yarns slippage followed by rupturing
SE300	507.1 (17)	Yarns slippage followed by rupturing
SE360	245.5 (7)	Yarns slippage

*Coefficients of variation in percentage terms are provided inside parentheses.

Table A 4. Prediction of saturated crack spacing at zero cycles.

Calculating tensile strength by	σ_{mu} [MPa]	$\tau_{f,PE}$ [MPa]	$\tau_{f,GT}$ [MPa]	X_{PE} [mm]	X_{GT} [mm]	$X_{PE}/X_{exp.}$ [%]	$X_{GT}/X_{exp.}$ [%]
compressive strength (f_m)	$0.3(f_m)^{2/3}$	2.16	1.83	96	113	95	112
flexural strength (f_{fl})	$\frac{0.06h_b^{0.7}}{1+0.06h_b^{0.7}} f_{fl}$			97	115	96	114
splitting strength (f_{sp})	$2.2(f_m)^{-0.18} f_{sp}$			90	106	89	105

f_m= 16.8 MPa; f_{fl}= 4.5 MPa; f_{sp}= 1.4 MPa; h_b: depth of flexural specimens (40 mm); $\tau_{f,PE}$: frictional strength of "single yarn"; $\tau_{f,GT}$: frictional strength of "single yarn+ transverse"; X_{PE} and X_{GT}: crack spacing predicted by $\tau_{f,PE}$ and $\tau_{f,GT}$.